

Shore protection by oblique seabed bars

Louis-Alexandre Couston¹, Mir Abbas Jalali²
and M.-Reza Alam¹

¹Department of Mechanical Engineering, University of California, Berkeley, CA, 94720, USA

²Department of Astronomy, University of California, Berkeley, CA, 94720, USA

Shore protection by small seabed bars was once considered possible because seafloor undulations strongly reflect surface waves of twice the wavelength by the so-called Bragg resonance mechanism. The idea, however, proved “unreliable” when Yu & Mei (*J. Fluid Mech.*, vol. 404, 2000, pp. 251-268) showed that a patch of longshore seabed bars adjacent to a reflective shore could result in larger waves at the shoreline than in the open ocean. Here we propose to revamp the Bragg resonance mechanism as a means of coastal protection by considering oblique seabed bars that divert, rather than reflect, shore-normal incident waves to the shore-parallel direction. The incident wave energy is therefore fully deflected to the sides, leaving a wake of decreased wave activity downstream of the patch. We show, via multiple-scale analysis supported by direct numerical simulations, that the creation of a large protected wake requires a bi-chromatic patch to deflect the incident waves to the shore-parallel direction. We demonstrate that the shore protection efficiency provided by this novel arrangement is not affected by reflection of leaked waves at the shoreline, nor by small frequency detuning.

1. Introduction

Coastal erosion, a threat to coastal communities and life, is accelerating because climate change has resulted in more frequent and stronger storms (c.f. Webster *et al.* 2005; Emanuel 2005). The Outer Banks of North Carolina are just one example of the areas that are very sensitive to storm conditions and that have sustained extensive property damage (Inman & Dolan 1989). The use of massive breakwaters as a means to mitigate storms of increasing severity remains the most common option despite well known imperfections: breakwaters adversely alter the coastal environment, require strong and costly foundations, need frequent maintenance due to cyclic load of the waves as well as liquefaction of the top part, and cause seabed soil subsidence at their foot besides potentially interfering with navigation.

In the 1980s, a promising alternative for coastal protection was put forward using a series of small man-made seabed-mounted corrugations to reflect the incident waves. The idea originated from the work of Davies (1982) who first studied the resonant interaction between free propagating surface waves and seabed undulations whose wavelengths are in a 2:1 ratio. The phenomenon is sometimes referred to as *Bragg reflection* or *resonance* due to its similarity with the selected reflection of X-rays from the surface of a crystal in solid state physics (see e.g. Pinsker 1978). The *strong* reflection of water waves by Bragg mechanism was shortly after investigated experimentally (c.f. Heathershaw 1982; Davies & Heathershaw 1984) as well as theoretically (see Mitra & Greenberg 1984; Mei 1985; Kirby 1986), and is now known to be of significant importance in the formation of nearshore sandbars and in the evolution of oceanic wave-field in littoral zones (e.g. Elgar *et al.* 2003).

The resonance condition discovered by Davies (1982) is in fact a special case of the

complete set of Bragg resonance conditions that can be obtained by regular perturbation of the potential flow equations for small corrugations (c.f. Liu & Yue 1998). At each order of the perturbation expansion, a set of resonated waves are obtained from the bottom boundary condition in which the seabed harmonics interact with the lower order wave solutions. The first order variations of the incident waves at or near resonance can then be obtained using multiple scales (e.g. Naciri & Mei 1988). For wave frequencies significantly different from the Bragg frequency, or in the presence of large amplitude bottom corrugations, higher-order theories such as Floquet theory become necessary to accurately predict solutions far from resonance, and to include evanescent modes and higher-order wave-bottom interactions (c.f. Yu & Howard 2012, and references therein).

In cases where closed-form solutions cannot be obtained, a wide range of numerical models are available to study water wave scattering by seabed topographies. These include the extended versions of the mild slope equations (e.g. Kirby 1986; Porter & Staziker 1995), the coupled mode approach (Athanasoulis & Belibassakis 1999; Belibassakis *et al.* 2001), the integral matching/discretized bottom method (O'Hare & Davies 1992; Seo 2014), the fully-nonlinear Boussinesq equation adjusted for rapid bottom undulations (see Madsen *et al.* 2006), and the high-order spectral method (e.g. Dommermuth & Yue 1987). Numerical investigations of Bragg scattering have helped explain several discrepancies between theory and experiments, including: the difference between the observed and predicted class II Bragg resonance frequency being due to evanescent modes (c.f. Guazzelli *et al.* 1992), and the resonant frequency downshift/upshift for the subharmonic/superharmonic class III Bragg condition due to high-order nonlinearity (c.f. Madsen *et al.* 2006).

The first-order reflection of incident waves by longshore seabed-mounted bars has been extensively studied theoretically, computationally, and experimentally to understand its effectiveness and limitations in shielding the shoreline (e.g. Kirby & Anton 1990; Bailard *et al.* 1990, 1992). The progress was however almost halted when Yu & Mei (2000*a*), based on earlier observations of Kirby & Anton (1990), showed that constructive interference of leaked waves trapped between the patch and a reflective shoreline could eventually result in significant wave amplification at the coast (c.f. figure 1a). The erosion of both natural sandbars and beaches being inevitable, shore protection by Bragg reflection was subsequently deemed unreliable. The importance of reflective boundaries on the slow modulation of the wave solution by Bragg reflection has also been demonstrated in wave tanks (c.f. Howard & Yu 2007; Weidman *et al.* 2015), and is at the basis of the Fabry-Perot resonance mechanism recently reported in the context of water waves (Couston *et al.* 2015).

Here we consider an arrangement of corrugations that can *deflect*, rather than reflect, shore-normal incident waves to the shore-parallel direction. We call this resonance mechanism *Bragg deflection*, to emphasize the contrast with Bragg reflection (since for the former the angle between the incident and resonated waves is less than or equal to 90°). The proposed patch of corrugations has a plane of symmetry, aligned with the direction of incident wave propagation, such that the incident wave energy gets diverted in the downstream to the sides of a protected wake (see figure 1b). One key advantage of the protection offered in the wake of such topography is that the protection efficiency is unaffected by coastal reflections, because waves reflected from the shoreline (either curved or straight) simply propagate back to the open ocean.

This manuscript considers the analysis of the *Bragg deflection* mechanism as a means of shore protection, and is organized as follows. The formulation of the problem, governing equations, and Bragg resonance conditions are presented in §2. In §3, using multiple-scale analysis, we investigate the protection provided by a monochromatic patch. The

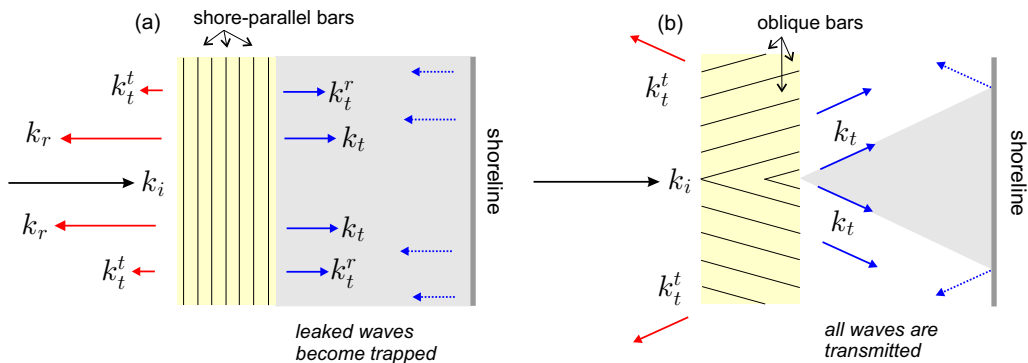


FIGURE 1. Schematics of shore protection by (a) Bragg reflection and (b) Bragg deflection. The gray-shaded area downstream of the corrugations represents the protected wake. (a) Most of the energy of an incident wave k_i , that arrives normal to a long patch of seabed bars, is reflected back (k_r). Nevertheless, a small part of the incident energy is still transmitted through the patch (k_t). The wave k_t , after reflecting back from the shoreline (dotted arrows), gets reflected strongly by the patch (k_t^r) with a small part transmitted back to the open ocean (k_t^t). The process repeats as the k_t^r wave reflected by the shoreline arrives again at the bars. Significant wave amplification can result from constructive wave interference between the trapped waves (i.e. k_t , k_t^r , k_t^{rr} , ...) depending on the distance between the patch and the shoreline (see Yu & Mei 2000a). (b) With oblique seabed bars, the incident wave k_i is deflected but also fully transmitted to the downstream (k_t). The k_t wave is then reflected by the shoreline and crosses back over the corrugated patch toward the open ocean.

advantages of a bi-chromatic patch for cases where the deflection angle is close to 90° are presented and discussed in §4. In §5, we validate the multiple-scale results by direct simulation, and analyze the effect of detuning and perpendicular deflection. Concluding remarks are finally drawn in §6.

2. Problem formulation

Consider the propagation of small amplitude waves on the surface of an incompressible, homogeneous and inviscid fluid of mean water depth h . We assume that the flow field is irrotational such that the velocity vector \vec{v} can be expressed as $\vec{v} = \nabla\Phi$, where Φ is the velocity potential. We define a Cartesian coordinate system (x, y, z) with x, y axis on the mean free surface and z axis positive upward. Governing equations and boundary conditions read

$$\nabla^2\Phi = 0, \quad -h + \zeta(x, y) \leq z \leq \eta(x, y, t), \quad (2.1a)$$

$$\Phi_{tt} + g\Phi_z + 2\nabla\Phi \cdot \nabla\Phi_t + \frac{1}{2}\nabla\Phi \cdot \nabla(\nabla\Phi \cdot \nabla\Phi) = 0, \quad z = \eta(x, y, t), \quad (2.1b)$$

$$\Phi_z = (-\nabla_h h + \nabla_h \zeta) \cdot \nabla_h \Phi, \quad z = -h + \zeta(x, y), \quad (2.1c)$$

where $\eta(x, y, t)$ is the free-surface elevation, g is the gravitational acceleration, $\nabla_h = (\partial_x, \partial_y)$ is the horizontal gradient operator, and $\zeta(x, y)$ is the height of the small bottom corrugations measured from the mean seabed depth ($z = -h$) such that the seabed is at $z = -h + \zeta$. Equation (2.1a) expresses mass conservation, (2.1b) is the combined free-surface boundary condition, and (2.1c) is the impermeable seabed kinematic boundary condition. The free-surface elevation $\eta(x, y, t)$ is obtained from the unsteady Bernoulli's

equation written on the free surface, i.e.,

$$\eta = -\frac{1}{g}(\Phi_t + \frac{1}{2}\nabla\Phi \cdot \nabla\Phi), \quad z = \eta(x, y, t). \quad (2.2)$$

Under the assumption of small surface slopes and small seabed corrugation slopes, i.e. $\nabla_h\eta, \nabla_h\zeta \sim \mathcal{O}(\epsilon) \ll 1$, a perturbation solution can be sought by expanding the velocity potential and free-surface elevation in a perturbation series, i.e.,

$$\Phi = \phi^{(1)} + \phi^{(2)} + \phi^{(3)} + \dots, \quad (2.3a)$$

$$\eta = \eta^{(1)} + \eta^{(2)} + \eta^{(3)} + \dots, \quad (2.3b)$$

where $(\phi^{(m)}, \eta^{(m)}) = \mathcal{O}(\epsilon^m)$. Substituting (2.3) in (2.1) and collecting terms of the same order, we obtain a series of equations of the form (c.f. Liu *et al.* 1998)

$$\nabla^2\phi^{(m)} = 0, \quad \text{in } -h \leq z \leq 0, \quad (2.4a)$$

$$\phi_{tt}^{(m)} + g\phi_z^{(m)} = F^{(m)}(\phi^{(1)}, \dots, \phi^{(m-1)}; \eta^{(1)}, \dots, \eta^{(m-1)}), \quad \text{on } z = 0, \quad (2.4b)$$

$$\phi_z^{(m)} = B^{(m)}(\phi^{(1)}, \dots, \phi^{(m-1)}; \zeta), \quad \text{on } z = -h. \quad (2.4c)$$

At each order m , (2.4) is a linear partial differential equation for $\phi^{(m)}$ with the right-hand-side being a nonlinear function of the solutions to the lower order problems. As a result, (2.4) can be solved sequentially starting from the leading order, i.e. the linear problem. The leading-order problem is unaffected by the bottom corrugations and has propagating wave solutions of the general form

$$\phi^{(1)} = \frac{A^{(1)}}{2} \frac{g \cosh[k(z+h)]}{\omega \cosh(kh)} e^{i(\mathbf{k}\cdot\mathbf{x}-\omega t)} + cc, \quad (2.5a)$$

$$\eta^{(1)} = i \frac{A^{(1)}}{2} e^{i(\mathbf{k}\cdot\mathbf{x}-\omega t)} + cc, \quad (2.5b)$$

where $A^{(1)}$ is the wave amplitude, cc stands for complex conjugate, and where ω and \mathbf{k} , i.e. the wave frequency and wavenumber vector, are related through the dispersion relation

$$\mathcal{D}(\omega; k = |\mathbf{k}|) \equiv \omega^2 - gk \tanh(kh) = 0. \quad (2.6)$$

At higher order $m > 1$, according to Fredholm alternative, if at least one of the forcing terms is secular, i.e. either $F^{(m)}$ or $B^{(m)}$ has an harmonic equal to one of the eigenvalues of the homogeneous problem, then no bounded solution can be found. At the second order, it is well known that $F^{(2)}$ can never satisfy such a condition. However, if the seabed has a component with the wavenumber vector \mathbf{k}_b such that

$$\mathbf{k} \pm \mathbf{k}_b = \mathbf{k}_r, \quad \text{and} \quad |\mathbf{k}_r| = |\mathbf{k}|, \quad (2.7)$$

then $B^{(2)}$ is secular and a wave with wavenumber \mathbf{k}_r will be *resonated*. In this case, the second order wave linearly grows in time, until it is too large for (2.3) to hold. A similar scenario happens also at the third order and $B^{(3)}$ becomes secular if the seabed is bi-chromatic with wavenumbers \mathbf{k}_{b_1} and \mathbf{k}_{b_2} such that

$$\mathbf{k} \pm \mathbf{k}_{b_1} \pm \mathbf{k}_{b_2} = \mathbf{k}_r, \quad \text{and} \quad |\mathbf{k}_r| = |\mathbf{k}|. \quad (2.8)$$

The resonance arising at the second order is called class I Bragg resonance, and the resonance arising at the third order (assuming no class I Bragg resonance between \mathbf{k} and \mathbf{k}_{b_1} or \mathbf{k}_{b_2}) is called class II Bragg resonance (c.f. Liu *et al.* 1998).

Since the class I Bragg resonance mechanism is more efficient at altering the incident

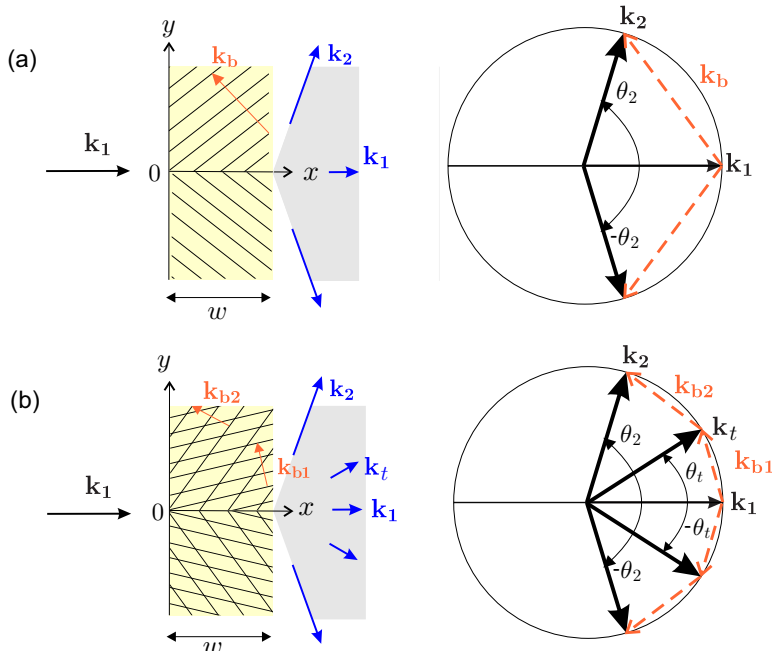


FIGURE 2. Schematics and Bragg resonance conditions for the deflection of $\mathbf{k}_1 = k_1 \hat{x}$ waves into \mathbf{k}_2 waves by (a) a monochromatic patch and (b) a bi-chromatic patch. The thin solid oblique lines represent the seabed bar crests whose corresponding bottom wavenumbers are denoted by \mathbf{k}_b for the monochromatic patch, and \mathbf{k}_{b1} and \mathbf{k}_{b2} for the bi-chromatic patch. The problem is symmetric with respect to the $y = 0$ plane such that significant wave energy reduction is expected in the shaded wake downstream of each patch. The class I Bragg resonance conditions $|\mathbf{k}_2| = |\mathbf{k}_1 \pm \mathbf{k}_b| = |\mathbf{k}_1|$ (c.f. equation (2.7)) for the monochromatic patch are shown in the upper and lower halves of the top circle, while the class I₂ Bragg resonance condition, i.e. $|\mathbf{k}_t| = |\mathbf{k}_1 \pm \mathbf{k}_{b1}| = |\mathbf{k}_1|$ and $|\mathbf{k}_2| = |\mathbf{k}_1 \pm \mathbf{k}_{b1} \pm \mathbf{k}_{b2}| = |\mathbf{k}_1|$ (c.f. §4, and note the contrast with class II in equation (2.8)) for the bi-chromatic patch are shown in the upper and lower halves of the bottom circle. Note that all wavenumbers correspond to leading-order wave modes and therefore the superscripts ⁽¹⁾ in (2.5) have been dropped.

wave-field than the high-order ones, in an attempt to protect the shore by diverting the incident waves away from a protected area, we will first consider the oblique class I Bragg resonance (c.f. figure 2a). It is, nevertheless, known that class I resonance is very weak for large deflection angles (i.e. for $\theta_2 \rightarrow \pi/2$ in figure 2a), and is degenerate at $\theta_2 = \pi/2$. As we will show in this manuscript, it is therefore advantageous, in order to deflect the normally incident waves toward the alongshore direction, to consider a superposition of two sets of oblique seabed bars (figure 2b). In order for the transfer of energy from the incident \mathbf{k}_1 wave to the target \mathbf{k}_2 wave to be efficiently mediated by the transitional \mathbf{k}_t wave, here we will consider that \mathbf{k}_1 and \mathbf{k}_{b1} satisfy a class I Bragg resonance condition, i.e. (2.7). In effect, the proposed superposition of corrugations thus involves two corrugation modes, but all interactions happen mainly at the second-order (in contrast to Class II Bragg resonance that happens at the third-order). Extending the nomenclature of Liu *et al.* (1998), we will refer to this scenario as a class I₂ Bragg resonance condition.

In the next two sections, we derive using multiple scales the slow evolution of the wave amplitudes near resonance for both the monochromatic (§3) and bi-chromatic patch (§4). The method of multiple scales is appropriate here because we only seek the leading-order solution for water waves propagating over small corrugations, and therefore the

superscripts $(1), (2), \dots, (m)$ in (2.3) can be dropped. Since our focus here is in nearshore areas where the waterdepth is typically smaller than the surface wavelength, the effect of directional spreading of incident waves will be neglected, which can be justified to first-order on the ground of wave refraction in shallow water.

3. Class I Bragg deflection for shore protection

Let us first consider a monochromatic patch with a plane of symmetry at $y = 0$, such that shore-normal incident waves get deflected to the sides of the x -axis by a set of oblique seabed bars (figure 2a). The bottom corrugations are taken as $\zeta(x, y)$ for $y > 0$ and $\zeta(x, -y)$ for $y < 0$, where

$$\zeta(x, y) = \begin{cases} \frac{d}{2}(e^{\mathbf{k}_b \cdot \mathbf{x}} + e^{-\mathbf{k}_b \cdot \mathbf{x}}), & 0 < x < w, \\ 0, & \text{otherwise.} \end{cases} \quad (3.1)$$

Under the class I Bragg resonance condition, i.e. $|\mathbf{k}_2| = |\mathbf{k}_1 + \mathbf{k}_b| = |\mathbf{k}_1|$, the incident and resonated wave amplitudes are of the same order. Their evolution, however, is slow for small bottom corrugations, and therefore can be decoupled from the fast variations of the carrier waves. We, therefore, consider a first-order velocity potential that accounts for both the incident (A_1) and resonated (A_2) waves according to

$$\phi^{(1)} = \frac{g}{\omega} \frac{\cosh[k_1(z+h)]}{\cosh(k_1 h)} \left[\frac{A_1(\bar{x}, \bar{y}, \bar{t})}{2} e^{i(\mathbf{k}_1 \cdot \mathbf{x} - \omega t)} + \frac{A_2(\bar{x}, \bar{y}, \bar{t})}{2} e^{i(\mathbf{k}_2 \cdot \mathbf{x} - \omega t)} \right] + cc. \quad (3.2)$$

The envelope amplitudes $A_{1,2}$ are functions of the slow space and time coordinates $(\bar{x}, \bar{y}, \bar{t}) \sim \epsilon(x, y, t)$ with $\epsilon \ll 1$. The governing equations for the slow evolution of $A_{1,2}$, obtained from multiple-scale analysis, read (Mei 1985)

$$\epsilon \frac{\partial}{\partial \bar{t}} A_1 + \epsilon \mathbf{C}_{\mathbf{g}_1} \cdot \bar{\nabla} A_1 + \epsilon (\bar{\nabla} \cdot \mathbf{C}_{\mathbf{g}_1}) \frac{A_1}{2} = i A_2 \Omega_c, \quad (3.3a)$$

$$\epsilon \frac{\partial}{\partial \bar{t}} A_2 + \epsilon \mathbf{C}_{\mathbf{g}_2} \cdot \bar{\nabla} A_2 + \epsilon (\bar{\nabla} \cdot \mathbf{C}_{\mathbf{g}_2}) \frac{A_2}{2} = i A_1 \Omega_c, \quad (3.3b)$$

where $\bar{\nabla} = (\partial/\partial \bar{x}, \partial/\partial \bar{y})$ and

$$\Omega_c = \frac{\omega d \mathbf{k}_1 \cdot \mathbf{k}_2}{2k_1 \sinh(2k_1 h)}, \quad \mathbf{C}_{\mathbf{g}_j} = \frac{\mathbf{k}_j \omega}{2k_1^2} \left[1 + \frac{2k_1 h}{\sinh(2k_1 h)} \right] = \frac{\mathbf{k}_j}{k_1} C_g. \quad (3.4)$$

Note that ϵ appears in front of all terms on the left-hand-side of equation (3.3), but that it is absent from the right-hand-side because the ripple amplitude $d \ll \mathcal{O}(k_1^{-1})$. This is simply due to the fact that we did not normalize the ripple amplitude d to keep it small compared to the other length scales of the system. The conservation of wave action equation, i.e.

$$\frac{\partial}{\partial \bar{t}} \left(\frac{|A_1|^2}{2} + \frac{|A_2|^2}{2} \right) + \bar{\nabla} \cdot \left(\mathbf{C}_{\mathbf{g}_1} \frac{|A_1|^2}{2} + \mathbf{C}_{\mathbf{g}_2} \frac{|A_2|^2}{2} \right) = 0, \quad (3.5)$$

deduced from (3.3), demonstrates that energy is exchanged between the two waves without any losses. We will make extensive use of the normalized amplitude variables

$$a_1^* = |A_1|/a_0, \quad a_2^* = |A_2| \sqrt{\cos \theta_2}/a_0, \quad (3.6)$$

throughout this manuscript, as they greatly simplify the analysis. For instance, (3.5) reduces to $a_1^{*2} + a_2^{*2} = 1$ when $\partial/\partial \bar{t} = \partial/\partial \bar{y} = 0$, which expresses the conservation of wave energy flux in the x -direction for a patch which is infinitely long in the y -direction and at the steady-state.

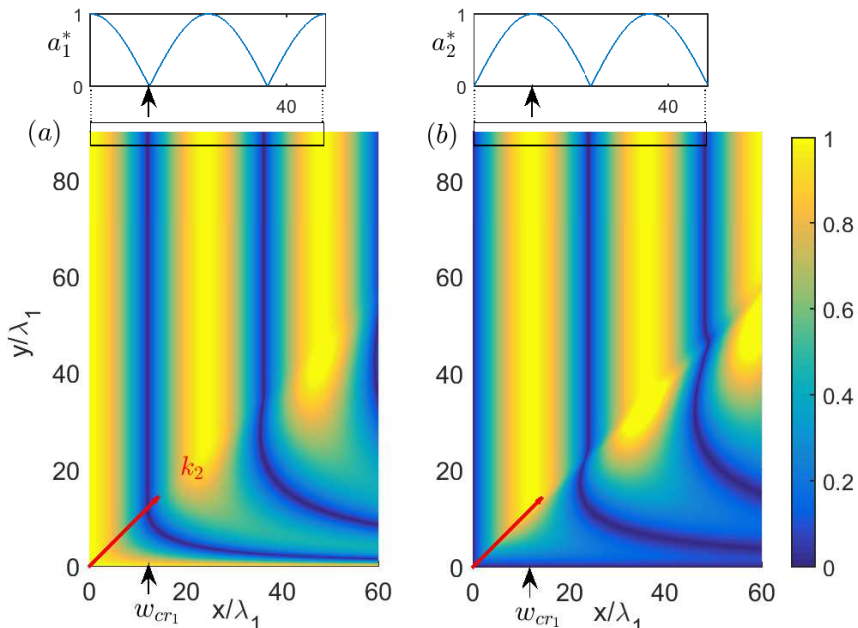


FIGURE 3. Normalized envelope amplitudes (a) a_1^* and (b) a_2^* as obtained from equation (3.3) with $\partial/\partial\bar{t} = 0$. The patch is semi-infinite, starting from $x = 0$, and the bottom corrugations are given by $\zeta(x, y)$ for $y > 0$ and by $\zeta(x, -y)$ for $y < 0$ (c.f. equation (3.1) with $w = +\infty$). The amplitude modulations far from the plane of symmetry (highlighted in the rectangles) are clearly the same as the y periodic solutions (shown by the solid lines in the top figures). We only show the amplitudes for $y > 0$ since the problem is symmetric with respect to the $y = 0$ axis. The small vertical arrows show the critical patch width w_{cr1} (such that $a_1^*(x = w_{cr1}) = 0$ far from $y = 0$), and the oblique arrows starting from the origin of each axis show the direction of propagation of the \mathbf{k}_2 waves. The physical parameters are $\theta_2 = \pi/4$, $k_1 h = 0.2$, $a_0/h = 10^{-3}$, $d/h = 0.1$. The simulation parameters are $\delta x/\lambda_1 = 0.05$ and $\delta y/\lambda_1 = 0.2$.

The system of equations (3.3) reduced under the assumption of steady-state and without detuning is not amenable to analytical treatment for a patch with a plane of symmetry (c.f. the solution derived for a corner patch of parallel seabed bars in Mei *et al.* 1988). As a result, here, we solve equations (3.3) assuming $\partial/\partial\bar{t} = 0$ numerically with an explicit finite-difference scheme. We use the Runge-Kutta fourth-order method for integration along the x axis (the x variable being similar to time here), and a second-order central finite-difference scheme in y . For the problem of shore protection, the incident wave has wavenumber $\mathbf{k}_1 = k_1 \hat{x}$ and the boundary conditions are $A_1 = a_0$, $A_2 = 0$ at $x = 0$ and $A_2 = 0$ at $y = 0$. The last condition enforces $A_1 = a_0$ at $y = 0$.

We show the normalized envelope amplitudes $a_{1,2}^*$ obtained over a monochromatic patch in figure 3. The patch is semi-infinite in the x -direction and the deflection angle is $\theta_2 = \pi/4$. While the behavior of the envelope amplitudes is relatively complex near the patch's plane of symmetry, their evolution for $y/\lambda_1 \gg 1$ becomes one-dimensional and periodic. The solution far from the patch's plane of symmetry can thus be obtained in closed-form, assuming $\partial/\partial\bar{y} = 0$, such that

$$\begin{pmatrix} A_1 \\ A_2 \end{pmatrix} = a_0 \begin{pmatrix} \cos K_c x \\ \frac{-i}{\sqrt{\cos \theta_2}} \sin K_c x \end{pmatrix}, \quad (3.7)$$

with

$$K_c = \Omega_c / (C_g \sqrt{\cos \theta_2}). \quad (3.8)$$

In figure 3, and from equation (3.7), we see that the incident wave energy far from the plane of symmetry first becomes fully transferred to the deflected wave mode at $x = w_{cr_1} = \pi / (2K_c)$. Therefore, w_{cr_1} is the critical monochromatic patch width since it is the shortest width that minimizes the amplitude of the incident waves in the downstream and away from the patch's plane of symmetry. At the end of a patch truncated at $x = w_{cr_1}$, most of the incident wave energy is deflected to the sides in the form of waves propagating at the angle θ_2 with respect to the x axis. Significant shore protection can thus be expected downstream of the patch, in a wake that looks like an isosceles triangle, with vertex angle equal to twice the angle (θ_2) of the Bragg resonated wave. As mentioned before, it is to be noted that class I Bragg resonance is degenerate at $\theta_2 = \pi/2$. It can be shown that $w_{cr_1} \rightarrow \infty$ when $\theta_2 \rightarrow \pi/2$, i.e., a monochromatic bar patch must be infinitely wide for a large deflection angle. The decreased efficiency of energy transfer between the incident and deflected waves for large θ_2 implies that a monochromatic patch cannot be used to protect large regions of a coast. This limitation is resolved in the next section as we show that a bi-chromatic patch, with the same total ripple amplitude as for the monochromatic one, is very efficient at deflecting incident waves for all θ_2 angles.

4. Class I₂ Bragg deflection for shore protection

Here we consider the case of a bi-chromatic patch for which the transfer of \mathbf{k}_1 wave energy to the \mathbf{k}_2 wave is mediated by a transitional Bragg resonated \mathbf{k}_t wave (c.f. figure 2b). We will show that the critical bi-chromatic patch width w_{cr_2} is much smaller than the critical monochromatic patch width w_{cr_1} for a large deflection angle θ_2 . We first study the behavior of the envelope amplitudes far from the patch's plane of symmetry to derive the critical patch width w_{cr_2} , and verify that the incident wave amplitude reaches zero downstream of the patch. We then solve the multiple-scale equations for the case of a patch with a plane of symmetry using the finite-difference scheme presented in §3.

4.1. Closed-form solution far from the patch's plane of symmetry

Here we derive the envelope equations for wave propagation over a bi-chromatic patch, i.e. with bottom corrugations of the form

$$\zeta = \frac{d_1}{2} (e^{\mathbf{k}_{b_1} \cdot \mathbf{x}} + e^{-\mathbf{k}_{b_1} \cdot \mathbf{x}}) + \frac{d_2}{2} (e^{\mathbf{k}_{b_2} \cdot \mathbf{x}} + e^{-\mathbf{k}_{b_2} \cdot \mathbf{x}}). \quad (4.1)$$

We assume that the incident wave number \mathbf{k}_1 satisfies both the class I and class II Bragg resonance conditions (which we refer to as class I₂), such that $\mathbf{k}_t \equiv \mathbf{k}_1 + \mathbf{k}_{b_1}$ and $\mathbf{k}_2 \equiv \mathbf{k}_t + \mathbf{k}_{b_2}$ are free waves that satisfy the dispersion relation (2.6). Since the wave \mathbf{k}_t is the first wave resonated, it can be shown using regular perturbation that initially the \mathbf{k}_t wave amplitude increases linearly in time while the \mathbf{k}_2 -wave growth is quadratic.

To obtain the multiple-scale equations for the bi-modal corrugation problem under the assumption of small bottom steepness, we consider a leading-order velocity potential of the form

$$\phi^{(1)} = \frac{g}{\omega} \frac{\cosh[k_1(z+h)]}{\cosh(k_1 h)} \left(\frac{A_1}{2} e^{i\mathbf{k}_1 \cdot \mathbf{x}} + \frac{A_t}{2} e^{i\mathbf{k}_t \cdot \mathbf{x}} + \frac{A_2}{2} e^{i\mathbf{k}_2 \cdot \mathbf{x}} \right) e^{-i\omega t} + cc. \quad (4.2)$$

The envelope amplitudes $A_{1,t,2}$ are functions of the slow coordinates $(\bar{x}, \bar{y}, \bar{t}) \sim \epsilon(x, y, t)$. Similar to the monochromatic problem, the evolutionary equations for $A_{1,t,2}$ are derived

from the so-called compatibility condition obtained upon inspection of the second-order problem in bottom steepness. The derivation is provided in Appendix I, and the final equations read

$$\epsilon \frac{\partial}{\partial \bar{t}} A_1 + \mathbf{C}_{\mathbf{g}_1} \cdot \epsilon \bar{\nabla} A_1 + \frac{A_1}{2} \epsilon \bar{\nabla} \cdot \mathbf{C}_{\mathbf{g}_1} = i A_t \Omega_1, \quad (4.3a)$$

$$\epsilon \frac{\partial}{\partial \bar{t}} A_t + \mathbf{C}_{\mathbf{g}_t} \cdot \epsilon \bar{\nabla} A_t + \frac{A_t}{2} \epsilon \bar{\nabla} \cdot \mathbf{C}_{\mathbf{g}_t} = i A_1 \Omega_1 + i A_2 \Omega_2, \quad (4.3b)$$

$$\epsilon \frac{\partial}{\partial \bar{t}} A_2 + \mathbf{C}_{\mathbf{g}_2} \cdot \epsilon \bar{\nabla} A_2 + \frac{A_2}{2} \epsilon \bar{\nabla} \cdot \mathbf{C}_{\mathbf{g}_2} = i A_t \Omega_2, \quad (4.3c)$$

where $\mathbf{C}_{\mathbf{g}_{1,t,2}}$ is given in (3.4) and with

$$\Omega_1 = \frac{\omega d_1 \mathbf{k}_1 \cdot \mathbf{k}_t}{2k_1 \sinh 2k_1 h}, \quad \Omega_2 = \frac{\omega d_2 \mathbf{k}_t \cdot \mathbf{k}_2}{2k_1 \sinh 2k_1 h}. \quad (4.4)$$

The governing equations (4.3) are valid for slow mean bottom variations, but for mathematical expediency, we will now assume that h is constant ($\Rightarrow \bar{\nabla} \cdot \mathbf{C}_{\mathbf{g}_{1,t,2}} = 0$). In practice, the effect of a mildly sloping beach does not change the Bragg resonance conditions which can be kept satisfied everywhere as long as the corrugation wavelength is adjusted to the local surface wavelength (c.f. Alam 2012a). The conservation of wave action equation, i.e.

$$\frac{\partial}{\partial \bar{t}} \left(\frac{|A_1|^2}{2} + \frac{|A_t|^2}{2} + \frac{|A_2|^2}{2} \right) + \bar{\nabla} \cdot \left(\mathbf{C}_{\mathbf{g}_1} \frac{|A_1|^2}{2} + \mathbf{C}_{\mathbf{g}_t} \frac{|A_t|^2}{2} + \mathbf{C}_{\mathbf{g}_2} \frac{|A_2|^2}{2} \right) = 0, \quad (4.5)$$

derived from (4.3), is the natural extension of (3.5) to the three-wave interaction problem. Defining the normalized transitional wave amplitude $a_t^* = |A_t| \sqrt{\cos \theta_t} / a_0$, (4.5) reduces to $a_1^{*2} + a_t^{*2} + a_2^{*2} = 1$ when $\partial / \partial \bar{t} = \partial / \partial \bar{y} = 0$ (c.f. (3.6) for $a_{1,2}^*$).

In the case of perfectly tuned waves far from the patch's plane of symmetry, a closed-form solution can be derived at the steady-state. Specifically, assuming $\partial / \partial \bar{t} = \partial / \partial \bar{y} = 0$ and enforcing the boundary conditions $A_1 = a_0$, $A_{t,2} = 0$ at $x = 0$, we obtain the solution

$$\begin{pmatrix} A_1 \\ A_t \\ A_2 \end{pmatrix} = \frac{a_0 K_1 K_2}{K_{12}} \begin{pmatrix} K_2 / K_1 + K_1 / K_2 \cos K_{12} x \\ i K_{12} / K_2 \sin K_{12} x \\ -1 + \cos K_{12} x \end{pmatrix}, \quad (4.6)$$

where

$$K_1 = \Omega_1 / (C_g \sqrt{\cos \theta_t}), \quad K_2 = \Omega_2 / (C_g \sqrt{\cos \theta_t \cos \theta_2}), \quad K_{12} = \sqrt{K_1^2 + K_2^2}. \quad (4.7)$$

The envelope amplitudes (4.6) are oscillatory over the patch, but the initial \mathbf{k}_1 wave does not necessarily cede all its energy to the \mathbf{k}_t or \mathbf{k}_2 wave. For $d_2 \neq 0$, the \mathbf{k}_1 wave amplitude reaches a minimum $A_1 = a_0 (K_2^2 - K_1^2) / K_{12}$ at $x = \pi / K_{12}$, which is zero if and only if

$$K_2 = K_1 \quad \Leftrightarrow \quad d_2 / d_1 = \sqrt{\cos \theta_2} \frac{\cos \theta_t}{\cos(\theta_2 - \theta_t)}, \quad (4.8)$$

in which case K_{12} reduces to

$$K_{12} = \sqrt{2} K_1. \quad (4.9)$$

Equation (4.8) describes the necessary balance between the efficiency of the $\mathbf{k}_1 \leftrightarrow \mathbf{k}_t$ and $\mathbf{k}_t \leftrightarrow \mathbf{k}_2$ Bragg interactions to achieve a synchronous energy transfer from \mathbf{k}_1 to \mathbf{k}_2 : if one of the deflection angles increases relative to the other, which diminishes the corresponding interaction efficiency, then the associated ripple amplitude should also

increase in order to balance the effect. The condition (4.8) is illustrated in figure 4a where we show the ratio d_2/d_1 as a function of θ_2 for four different transitional angles. Clearly d_2/d_1 decreases when θ_t increases since the $\mathbf{k}_t \leftrightarrow \mathbf{k}_2$ Bragg interaction becomes more effective with decreasing $\theta_2 - \theta_t$. The ratio d_2/d_1 also decreases almost monotonically with increasing θ_2 since the \mathbf{k}_2 wave's time spent over the patch, or, in other words, the number of wave-seabed interactions, scales with $\sqrt{1 + \tan^2 \theta_2}$. For instance, when \mathbf{k}_1 waves travel one unit distance in the x direction, \mathbf{k}_2 waves only move by $\cos \theta_2$ in x .

When (4.8) is satisfied, all the \mathbf{k}_1 -wave energy transfers to the \mathbf{k}_2 waves after traveling the distance $w_{cr_2} = \pi/K_{12}$, which we shall refer to as the critical bi-chromatic patch width. For a fixed θ_2 and a fixed normalized total ripple amplitude $(d_1 + d_2)/h$, the critical bi-chromatic patch width has a unique minimum at $\theta_t = \theta_t^{opt}$, such that θ_t^{opt} maximizes K_{12} as given by (4.9). The variations of θ_t^{opt} as a function of θ_2 are shown in figure 4b.

In practice, θ_t^{opt} can be approximated by $\theta_2/2$ since the corresponding critical patch widths are nearly the same, as can be seen in figure 4c from the overlap of the w_{cr_2} curve obtained for θ_t^{opt} with the dashed curve obtained for $\theta_t = \theta_2/2$. Figure 4c also shows the critical patch width w_{cr_1} for a monochromatic patch. Interestingly, w_{cr_2} is greater than w_{cr_1} for relatively small deflection angles because we assumed $d_2 \neq 0$ in deriving (4.8). Assuming $d_2 = 0$, we would get $w_{cr_2} = w_{cr_1}$ since both patches would involve only one Bragg interaction. Since $w_{cr_1} = w_{cr_2}$ at $\theta_2 \sim 11\pi/25$ for $\theta_t = \pi/2$, as can be seen from figure 4c (intersection of dash-dash line with 1-corr. curve), the bi-chromatic patch becomes significantly more efficient for shore protection for deflection angles $\theta_2 > 11\pi/25$.

While the values predicted by multiple-scale for d_2/d_1 (see figure 4a), θ_t^{opt} (figure 4b), and w_{cr_2} (figure 4c) are valid for most θ_2 , the trends in the limit where $\theta_2 \rightarrow 0$ or $\theta_2 \rightarrow \pi/2$ may be inaccurate. Indeed, $\theta_2 \sim 0$ implies seabed bar crests almost parallel to \mathbf{k}_1 , which contradicts the multiple scale assumption of a rapidly varying waterdepth in x . The configuration $\theta_t \sim \theta_2$ also violates the multiple-scale assumption since in this case some of the seabed bar crests become almost parallel to \mathbf{k}_t . The case of $\theta_2 = \pi/2$ requires also special care, primarily because the incident wave energy cannot be transferred to the target \mathbf{k}_2 waves at steady-state assuming y invariance. Shore protection by perpendicular deflection, for which $\theta_2 = \pi/2$, will be discussed in details in §5 using direct simulation.

4.2. Effect of the patch's plane of symmetry

We now take into account the patch's plane of symmetry, that is, we consider bottom corrugations given by $\zeta(x, y)$ in (4.1) for $y > 0$, and by $\zeta(x, -y)$ for $y < 0$. We solve the system of equations (4.3) with the same finite-difference scheme used for the case of a monochromatic patch in §3, and we enforce the synchronization condition (4.8), such that full energy transfer from the \mathbf{k}_1 waves to the \mathbf{k}_2 waves is achieved far from the plane of symmetry. The incident wave has wavenumber $\mathbf{k}_1 = k_1 \hat{x}$ and the boundary conditions are $A_1 = a_0$, $A_{t,2} = 0$ at $x = 0$ and $A_{t,2} = 0$ at $y = 0$. The last condition forces also $A_1 = a_0$ at $y = 0$.

We show $a_{1,t,2}^*$ obtained for a semi-infinite patch in x direction with $\theta_2 = 7\pi/15$ and $\theta_t = \theta_2/2$ in figure 5. We have marked in figure 5 the directions of the \mathbf{k}_t and \mathbf{k}_2 waves by oblique arrows starting from the origin of each axis. Far from $y = 0$, the problem becomes one-dimensional and the separation wavelength between two successive crests of the \mathbf{k}_1 or \mathbf{k}_2 wave envelope is $2w_{cr_2} = 2\pi/K_{12}$ as predicted by (4.6) (see the figures on top of each frame that show the y -invariant solutions).

The wave patterns near $y = 0$ show the remarkable complexity of the three-wave interaction process near the $y = 0$ plane of symmetry. Generally, wave amplitudes near

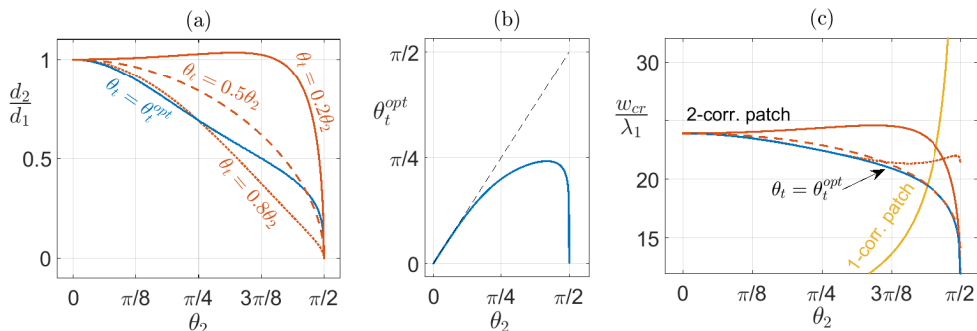


FIGURE 4. (a) Ratio of the corrugation amplitudes d_2/d_1 as a function of θ_2 , such that full energy transfer is achieved between the \mathbf{k}_1 wave and the \mathbf{k}_2 wave at the end of a patch of width $w = w_{cr_2} = \pi/K_{12}$ (c.f. (4.8)). The four different curves correspond to different transitional angles θ_t . (b) The unique optimal transitional angle θ_t^{opt} , as a function of θ_2 , which minimizes the critical patch width w_{cr_2} , for a fixed total ripple amplitude $(d_1 + d_2)/h = 0.12$ and normalized water depth $k_1 h = 0.2$, and provided that (4.8) is satisfied. (c) Plot of the critical patch width w_{cr_2} for bi-modal corrugations (2-corr. patch) for various transitional angles (same line-style notation as in figure 4a). We also plot the critical patch width for a monochromatic patch $w_{cr_1} = \pi/(2K_c)$ (1-corr. patch) for which the corrugation amplitude is $d/h = 0.12$ (c.f. (3.8)). The critical monochromatic patch width becomes rapidly much larger than the critical bi-chromatic patch width when $\theta_2 \rightarrow \pi/2$.

$y = 0$ are smaller further down the patch due to the deflection. The qualitative behavior of waves in each one of the three distinguishable regions (i.e. $y/x > \tan \theta_2$, $\tan \theta_2 > y/x > \tan \theta_t$, and $y/x < \tan \theta_t$), changes with a change in θ_t or θ_2 . It is to be noted that once we introduce a plane of symmetry at $y = 0$, neither a_1^* nor a_t^* become uniformly zero in y at $x = w_{cr_2}$ (c.f. the near field $y \sim 0$ and $x = w_{cr_2}$ in figure 6a). Therefore, even though the critical patch width minimizes wave energy in the protected wake, there will always be leaked waves emanating near $y = 0$ at the end of the patch and propagating to the downstream.

Figure 6 shows the variations of the normalized wave amplitudes $a_{1,t,2}^*$ as functions of y at the end of a bi-chromatic patch truncated at $x = w_{cr_2}$ for $\theta_2 = 11\pi/25$ (a,b,c) and $\theta_2 = 7\pi/15$ (d,e,f). For comparison, we also plot $a_{1,2}^*$ for a monochromatic patch ending at $x = w_{cr_1}$ (dash-dotted line). Clearly, the bi-chromatic patch achieves a much better reduction in the incident wave amplitude everywhere (c.f. figures 6a,d). The \mathbf{k}_1 wave amplitude drops much more quickly in y for the bi-chromatic patch, because some of its energy is stored in the hump of \mathbf{k}_t wave energy seen in figures 6b,e (note that the horizontal axis is on a logarithmic scale truncated at 10^{-1}). Using two corrugation modes instead of one, thus not only decreases the critical patch width for large θ_2 , but also spreads out a fraction of the energy leaked near $y = 0$ further to the sides in the form of \mathbf{k}_t waves. Interestingly, the location of the second hump of \mathbf{k}_1 wave energy (figures 6a,d) scales with $1/\sqrt{\cos \theta_t}$, which suggests that the $\mathbf{k}_1 \leftrightarrow \mathbf{k}_t$ wave energy exchange is partially oscillatory in y with a period similar to the period of oscillation in the x direction (c.f. K_{12} in (4.9)).

Since the widths of the mono- and bi-chromatic patches are critical, we obtain $a_1^* \sim 0$ and $a_2^* \sim 1$ for $y/\lambda_1 \gg 1$ in figures 6c,f. In both cases we also observe that the \mathbf{k}_2 wave gains energy more rapidly for the smaller θ_2 angle: for instance, considering the case of $\theta_t = \theta_2/2$ (solid lines), we find that $a_2^* = 0.9$ at $y/\lambda_1 = 80, 134$ for $\theta_2 = 11\pi/25, 7\pi/15$. This suggests that there might be a compromise to be found between deflecting at a very

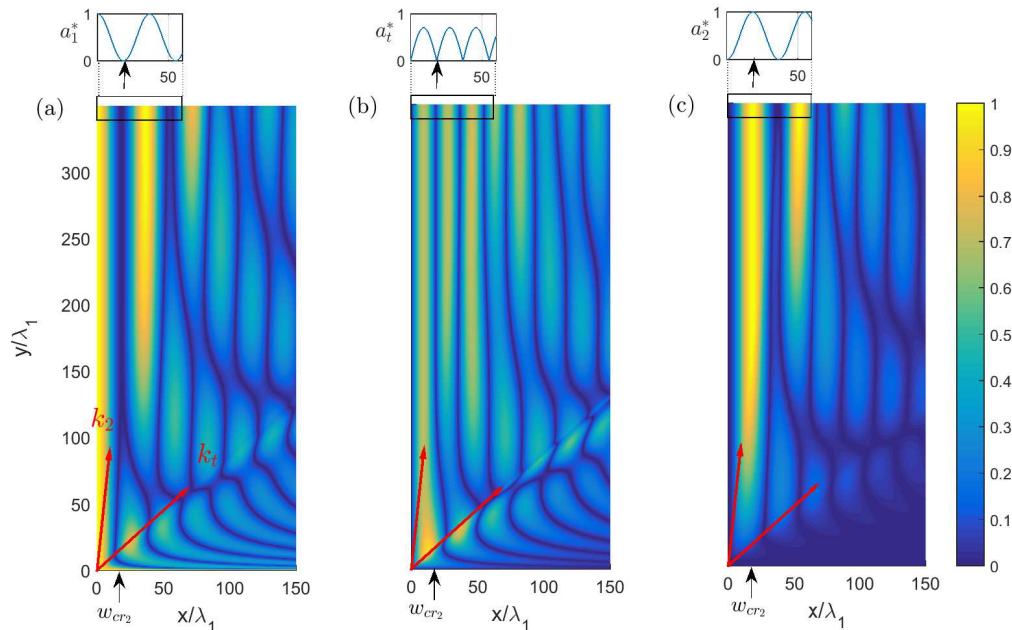


FIGURE 5. Normalized envelope amplitudes (a) a_1^* , (b) a_t^* and (c) a_2^* , over a bi-chromatic patch, as obtained from equation (4.3) with $\partial/\partial \bar{t} = 0$. The patch is semi-infinite, starting from $x = 0$ onward, and the bottom corrugations are given by $\zeta(x, y)$ for $y > 0$ and by $\zeta(x, -y)$ for $y < 0$ (c.f. equation (4.1)). The amplitude modulations far from the plane of symmetry (i.e. highlighted in the rectangles) are clearly similar to the y -invariant solutions (shown in the top figures). We only show the amplitudes for $y > 0$ since the problem is symmetric with respect to the $y = 0$ plane. The small vertical arrows show the critical patch width w_{cr2} . The physical parameters are $\theta_2 = 7\pi/15$, $\theta_t = \theta_2/2$, $k_1 h = 0.2$, $a_0/h = 10^{-3}$, $(d_1 + d_2)/h = 0.12$, with (4.8) satisfied. The simulation parameters are $\delta x/\lambda_1 = 0.05$ and $\delta y/\lambda_1 = 0.2$.

large angle and minimizing the energy content of the transmitted wave beams. The effect of the transitional angle on the amount of energy captured by the \mathbf{k}_2 wave is relatively minor, as can be seen from the overlap of the a_2^* curves obtained for $\theta_t = 0.2\theta_2, 0.5\theta_2, 0.8\theta_2$ in figures 6c,f.

As a note of caution, we remark that the variations of the \mathbf{k}_1 wave amplitude are relatively fast close to $y = 0$ (indeed a_1^* drops from 1 to about 0 in just five wavelengths for $\theta_t = 0.5\theta_2$ in figure 6a), such that the assumption of multiple scales becomes violated. Nonetheless, a qualitatively similar behavior will be demonstrated in the next section when solving the full potential flow equations.

5. Direct simulation

A realistic consideration of a patch of seabed bars for coastal protection must take into account all resonance and near-resonance interactions as well as the effect of bottom discontinuities and boundaries. As a general approach to address these, here we use a direct simulation scheme of high-order spectral method. The high-order spectral scheme solves the potential flow equation (2.1) assuming that the solution can be expressed in terms of a convergent series (c.f. Zakharov 1968). It can take up to an arbitrary order of nonlinearity M (i.e. number of terms in the perturbation expansion, typically

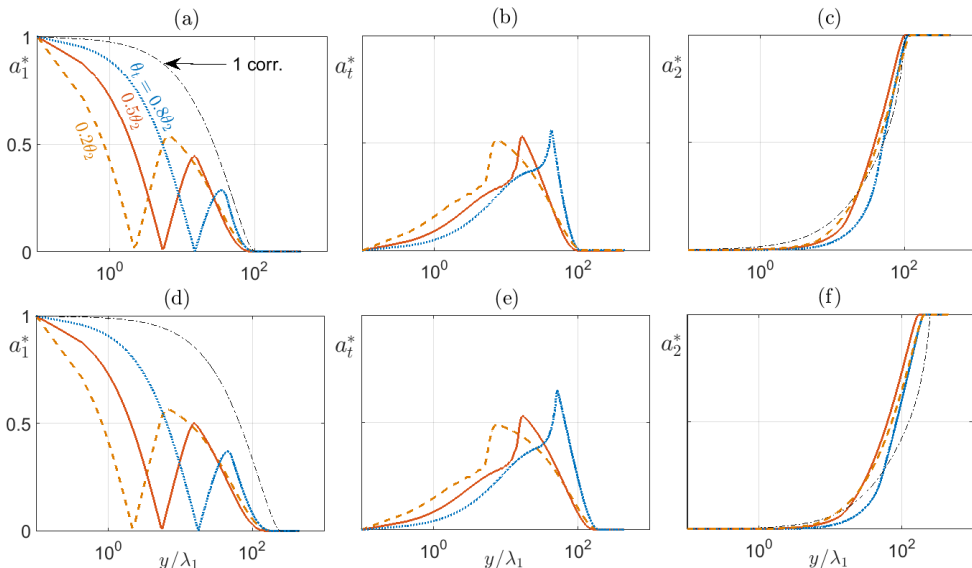


FIGURE 6. Normalized envelope amplitudes a_1^* , a_t^* , a_2^* at the end of a patch truncated at the critical patch width $x = w_{cr2}$ (indicated by a small vertical arrow in figure 5) for $\theta_2 = 11\pi/25$ (plots (a), (b), (c)) and $\theta_2 = 7\pi/15$ (plots (d), (e), (f)). The x -axis is on a logarithmic scale so as to show details near the plane of symmetry. Solid, dashed, and dotted lines represent results obtained for $\theta_t = 0.2\theta_2, 0.5\theta_2, 0.8\theta_2$ respectively. The dash-dotted lines show the \mathbf{k}_1 -wave and \mathbf{k}_2 -wave amplitudes at the end of a monochromatic patch of width w_{cr1} . Physical and simulation parameters are the same as those in figure 5.

$M \sim \mathcal{O}(10)$) and a high number of wave modes N (typically $N \sim \mathcal{O}(10,000)$). The method was first formulated by Dommermuth & Yue (1987) and West *et al.* (1987) to model nonlinear wave-wave interactions in deep water. It was then extended to the problems of wave-topography interactions in finite depth (Liu *et al.* 1998; Alam *et al.* 2010, 2011), two-layer density stratified fluids (Alam *et al.* 2009*a,b*), and wave-viscoelastic-seabed interactions (Alam 2012*a*). The scheme has already undergone extensive convergence tests as well as validations against experimental and other numerical results (e.g. Toffoli *et al.* 2010; Alam 2012*b*).

5.1. Cross-validation

We compare the direct simulation and multiple-scale results of a normal-to-shore monochromatic wavetrain impinging on a bi-chromatic patch with a $y = 0$ plane of symmetry. We select the dimensionless wavenumber $k_1 = 110$, such that 110 waves of wavelength λ_1 can fit in the numerical domain $x \in [0, 2\pi[$. We use the same parameters as in figures 5 and 6(d,e,f) such that $\theta_2 = 7\pi/15$, $\theta_t = \theta_2/2$, $k_1 h = 0.2$, $a_0/h = 10^{-3}$, and $(d_1 + d_2)/h = 0.12$ with (4.8) satisfied. The seabed bars are laid out from $x/\lambda_1 = 0$ to $x/\lambda_1 = w_{cr2}/\lambda_1 = 18.3$ and therefore the patch width is critical. The generation of the initial waves coming from $x = -\infty$, and the radiation conditions for waves leaving the domain (at $x = +\infty$ or $y = \pm\infty$) are enforced using a numerical wavemaker and damping layers. This procedure significantly attenuates the additional water-wave scattering at the lateral boundaries of the patch (which is finite in the numerical domain), such that a good agreement can be expected between theory and direct simulation (the effect of the patch's finite transverse length, here in y , was studied in Magne *et al.* 2005).

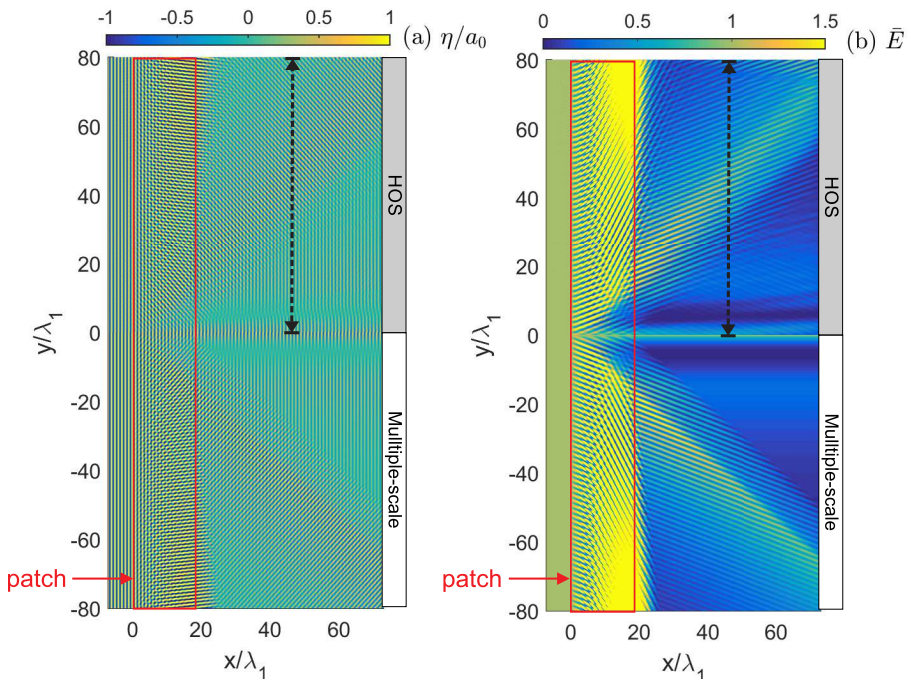


FIGURE 7. (a) Free-surface elevation η/a_0 and (b) time-averaged energy (c.f. (5.1)) at the steady-state obtained from direct simulation (upper plots $y > 0$) and multiple-scale analysis (lower plots $y < 0$; c.f. equations (4.3)). A monochromatic wave-train incident from $x = -\infty$ impinges on a bi-chromatic patch with parameters $\theta_2 = 7\pi/15$, $\theta_t = \theta_2/2$, $k_1 = 110$ (dimensionless), $k_1 h = 0.2$, $(d_1 + d_2)/h = 0.12$ (with d_2/d_1 given by (4.8)), $a_0/h = 10^{-3}$ (c.f. figure 2b). The seabed bars occupy the space between $x = 0$ and $x/\lambda_1 = w_{cr2}/\lambda_1 = 18.3$ such that all the incident \mathbf{k}_1 wave energy transfers to the target \mathbf{k}_2 wave away from the patch's plane of symmetry $y = 0$. The direct simulation parameters are $\delta x/\lambda_1 = \delta y/\lambda_1 = 1/9$ and $\delta t/T_1 = 1/32$, and the resolution of the multiple-scale solution is the same as in figure 5. The vertical dashed lines show the transects where we plot the maximum free-surface elevation in figure 8.

Figure 7a shows the normalized wave elevation η/a_0 when steady state is reached. The plot is split into two parts, with the lower part ($y < 0$) obtained from the semi-analytical solution (c.f. §4), and with the upper part ($y > 0$) obtained from direct simulation. As can be seen, analytical and computational results endorse each other, with the same features already described in §4 standing out: (i) the incident waves arrive unaffected upstream of the patch from $x = -\infty$, (ii) the complex pattern due to the three-wave interactions over the patch becomes y -invariant away from the centerline (i.e. $|y| \gg \lambda_1$), (iii) two beams of \mathbf{k}_1 wave energy propagate near $y = 0$ downstream of the patch (one near the center at $y \sim 0$, and the other at $y \sim 15\lambda_1$), (iv) a beam of \mathbf{k}_t wave energy emanates from the end of the patch at $y \sim \pm 19\lambda_1$.

The protection provided by the bi-chromatic patch can be further highlighted by looking at the time-averaged energy

$$\bar{E}(x, y) = \frac{1}{a_0^2/2} \int_{t_0}^{t_f} \eta^2(x, y, t) \frac{dt}{t_f - t_0}, \quad (5.1)$$

where the pre-factor in (5.1) is inversely proportional to the averaged wave energy that would be obtained without the seabed bars. It should be noted that (5.1) is the first-

order normalized wave energy, and that it includes contributions from both the kinetic and potential wave energy, which are equal. The time integration is performed when the system reaches steady-state with $t_0/T_1 = 140$ and $t_f/T_1 = 170$. A good agreement is obtained for \bar{E} in figure 7b between the direct simulation (lower half) and the multiple-scale results (upper half). The features described for figure 7a also appear in figure 7b and are in fact strongly enhanced (e.g. \mathbf{k}_1 and \mathbf{k}_t wave beams). The rapid variations of wave energy are due to the formation of a standing wave pattern downstream of the patch (e.g. along the \mathbf{k}_t wave beam direction) resulting from the superposition of \mathbf{k}_1 and \mathbf{k}_t waves. The strongest energy reduction is about 99% (for both direct simulation and multiple-scale) and is achieved within the stripe of width $2\lambda_1$ centered on $y = \pm 5\lambda_1$.

5.2. Effect of detuning and protection efficiency

To quantify the effect of frequency detuning on the shore protection efficiency, we calculate the maximum free-surface elevation $\eta^* = \max |\eta|/a_0$ (in time) with and without detuning along the y -axis at a virtual shoreline (no reflection considered) that is assumed $\Delta x = 26\lambda_1$ downstream of the patch (i.e. along the dashed lines in figure 7). The incident wave frequency is $\omega = \omega_1 + \varpi$ where ω_1 is the perfectly tuned wave frequency and $\varpi \ll \omega_1$ is the detuning parameter. The corresponding wavenumber detuning κ , such that $k = k_1 + \kappa$, is obtained from $\varpi = C_g \kappa$. Similar to the case of class I Bragg reflection (see e.g. Mei 1985), we normalize the detuning frequency by the characteristic long time scale of the system $\Omega_{12} = C_g K_{12}$ (c.f. (4.7)). The normalized detuning ϖ/Ω_{12} is therefore represents the strength of detuning, which suggests that shorter waves are more strongly affected by detuning than longer waves (a detailed analysis of detuning for a bi-chromatic patch infinitely long in the y -direction is provided in Appendix II).

The Result of our numerical experiments on the effect of detuning is presented in figure 8. In the absence of detuning, i.e. $\varpi = 0$, a global minimum of η^* for both direct simulation and multiple-scale is observed: this minimum in η^* corresponds to the minimum of incident wave amplitude a_1^* at the end of the patch as seen in figure 6d (dotted line at $y/\lambda_1 \sim 6$). The large standing-wave oscillations seen for $y/\lambda_1 > 25$ are, as mentioned previously, due to the superposition of the leaked \mathbf{k}_1 and \mathbf{k}_t waves. Of course, the superposition would not occur if we were to observe η^* further downstream of the patch since the \mathbf{k}_t beams of energy propagate progressively away from the $y = 0$ plane of symmetry to which the \mathbf{k}_1 beams of energy are confined. The maximum free-surface elevation obtained from the direct simulation matches well with the multiple-scale solution except for a small local peak near $y = 0$ and for the small oscillations from $y = 0$ to $y = 25\lambda_1$, which are both due to wave energy spreading.

The effect of detuning on the maximum free-surface elevation is strongest away from the $y = 0$ plane of symmetry. There still is a global minimum near $y = 0$ for $\varpi/\Omega_{12} = 3.7$ but η^* reaches a unitary value (which corresponds to no wave amplitude reduction) near $y = 15\lambda_1$ with oscillations farther out to the sides again due to the superposition of \mathbf{k}_1 and \mathbf{k}_t waves. The wave-field away from $y = 0$ changes radically because the second interaction of the two-steps Bragg resonance mechanism, which is key to reducing the incident wave mode energy far from the plane of symmetry, is more strongly impacted than the first Bragg interaction. The fact that detuning affects the successive Bragg interactions cumulatively is shown in Appendix II (figures 12,13) for an infinitely long patch.

Quantitative differences between direct simulation and multiple-scale results are in general expected and obtained here in figure 8 because multiple-scale neglects higher-order wave-bottom interactions, wave-wave nonlinearities, and bottom discontinuities (obtained at the beginning and end of the patch), which can produce evanescent modes.

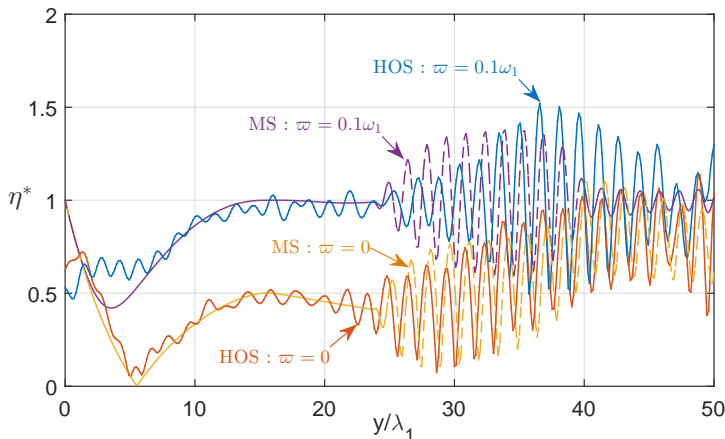


FIGURE 8. Effect of detuning on the normalized maximum free-surface elevation $\eta^* = \max |\eta|/a_0$ at a distance $\Delta x/\lambda_1 = 26$ downstream of the patch (i.e. along the dashed lines in figure 7). The wavenumber for which the patch is designed is $k_1 = 70$ and the detuning parameter is $\varpi/\omega_1 = 0$ for the lower two curves and $\varpi/\omega_1 = 0.1$ (or $\varpi/\Omega_{12} = 3.7$) for the upper two curves. Other physical parameters are as in figure 7. The direct simulation (HOS) parameters are $\delta x/\lambda_1 = \delta y/\lambda_1 = 1/7.3$ and $\delta t/T_1 = 1/32$, and the resolution of the multiple-scale solution (MS) is the same as in figure 5. Detuning clearly results in a larger maximum wave amplitude downstream of the patch.

For instance, resolving accurately subharmonic resonances due to multiple bottom components, which could be of significance in the case of large detuning, requires theories that include higher-order wave-bottom interactions (c.f. Guazzelli *et al.* 1992; Yu & Howard 2012). Despite the simplifying assumptions of multiple-scale analysis, we see that the comparison in figure 8 is good almost everywhere in the domain, with or without detuning. The small discrepancies between the two methods is of course higher for the detuned waves, which is consistent with the fact that multiple-scale performs best at perfect resonance, i.e. in the absence of detuning.

To further assess the efficiency of the Bragg deflection mechanism, as well as how it is affected by detuning, we now define a protection efficiency variable \mathcal{P} , where

$$\mathcal{P}(x, y) = 1 - \frac{1}{y} \int_0^y \bar{E}(x, \tau) d\tau. \quad (5.2)$$

The protection efficiency \mathcal{P} measures the y -average wave energy reduction (with \bar{E} obtained at steady-state and given in (5.1)) on a line parallel and downstream of the patch's trailing edge. Figure 9a shows \mathcal{P} over a relatively large domain, i.e. from $y = 0$ to $y = 350\lambda_1$, with \bar{E} evaluated at the distance $\Delta x = 26\lambda_1$ downstream of the patch. Figure 9b is a close-up with direct simulation results (dashed lines), to show that the multiple-scale predictions are reasonably accurate, even with 10% detuning.

The protection efficiency \mathcal{P} for perfectly tuned waves (i.e. $\varpi = 0$) is as high as 88% at $y = 270\lambda_1$, meaning that only 12% of the incident wave energy makes it inside the protected wake behind the patch. From $y \sim 270\lambda_1$ farther out to the sides, \mathcal{P} starts decreasing because the deflected \mathbf{k}_2 waves, which captured most of the incident wave energy, propagate within the semi-infinite space $y > x/\cos\theta_2$ outside of the protected

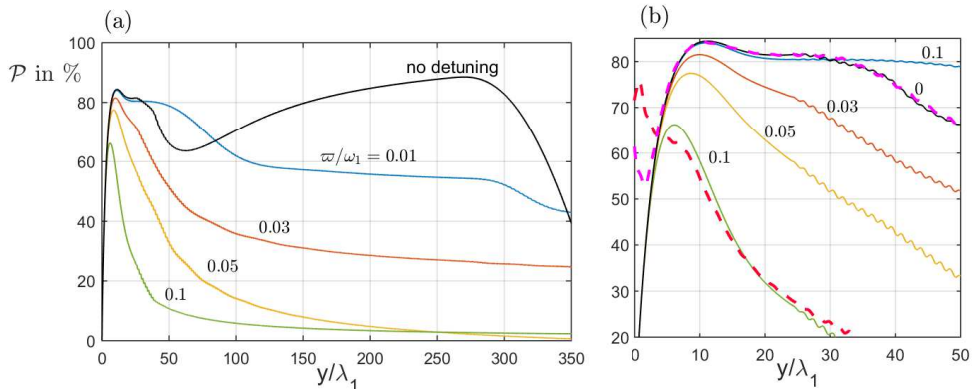


FIGURE 9. (a) Protection efficiency \mathcal{P} (5.2) with and without detuning ($\varpi/\omega_1 = 0, 0.01, 0.03, 0.05, 0.1$ which corresponds to $\varpi/\Omega_{12} = 0, 0.37, 1.1, 1.8, 3.7$) at a distance $\Delta x = 26\lambda_1$ downstream of the patch (i.e. at $x = w_{cr2} + 26\lambda_1$, which is along the dashed line in figure 7). The results are obtained from multiple-scale analysis. (b) Close-up with direct simulation results added for $\varpi/\omega_1 = 0, 0.1$ (dashed lines). The physical and simulation parameters other than ϖ are the same as those in figure 8.

wake, which includes the half line $y > 270\lambda_1 > 26\lambda_1/\cos(7\pi/15)$. As already discussed, the protection efficiency decreases rapidly with an increase in ϖ away from $y = 0$ since the two-step Bragg deflection mechanism is quite sensitive to detuning. Detuning affects transmitted waves (as in Bragg deflection) more strongly than reflected waves, because transmitted waves have an oscillatory behavior over the corrugations: detuning not only diminishes wave-bottom interactions but also changes the critical patch width where the incident wave amplitude reaches a minimum. Nonetheless, we can see that significant wave amplitude reduction is still achieved over a large domain with some small detuning.

5.3. Perpendicular deflection

In this section we investigate numerically the special case of shore-normal incident waves (with wavenumber $\mathbf{k}_1 = k_1\hat{x}$) being deflected by 90 degrees into shore-parallel resonated waves ($\mathbf{k}_2 = \pm k_2\hat{y}$, c.f. figure 2b). Assuming perfectly tuned incident waves, we first show in figure 10 that the averaged wave energy (5.1) is significantly decreased in the wake of such a patch. A bi-chromatic patch can therefore deflect incident waves to the shore-parallel direction, and offer shore protection near the patch's plane of symmetry. The physical parameters in figure 10 are the same as those in 7 (except for $\theta_2 = \pi/2$ in figure 10), such that the patch width in figure 10 is not critical. Nonetheless, wave reduction is obtained in the wake near the patch's plane of symmetry regardless of its width.

Far from the plane of symmetry where the solution is expected to be y -invariant, the synchronization condition (4.8) suggests that the bi-chromatic patch should be turned into a monochromatic patch since we get $d_2/d_1 \rightarrow 0$ when $\theta_2 \rightarrow 0$. However, as was mentioned earlier, the degeneracy of the Bragg resonance condition prevents a monochromatic patch from deflecting incident waves by a $\theta_2 = \pi/2$ angle. Therefore the solution (4.4) is not valid for perpendicular deflection and we should still consider a bi-chromatic patch (with $d_{1,2} \neq 0$). Let us now suppose that the envelope amplitudes need not be continuous at the patch boundaries, i.e. at $x = 0$ or $x = w$. Then, the steady-state ($\partial/\partial\bar{t} \equiv 0$) y -invariant ($\partial/\partial\bar{y} \equiv 0$) solution of equations (4.3) with $\theta_2 = \pi/2$ is obtained

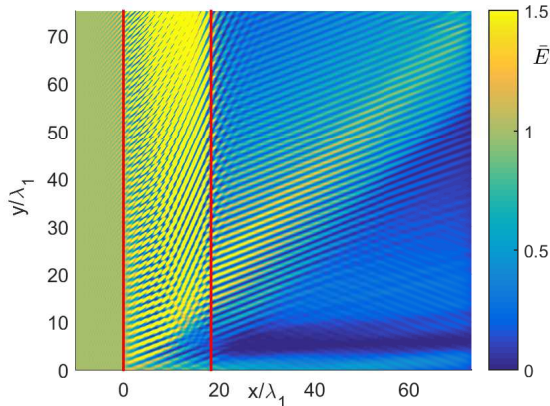


FIGURE 10. Time-averaged energy \bar{E} (c.f. (5.1), $t_0/T_1 = 140$, $t_f/T_1 = 170$) obtained from direct simulation for a patch with a plane of symmetry at $y = 0$. The physical and simulation parameters are identical to those in figure 7 except for the deflection angle which is now set to $\theta_2 = \pi/2$. The energy distribution is symmetric with respect to the $y = 0$ axis which is why we only show the upper half plane $y > 0$. The red lines show the extent of the corrugated patch in the x direction.

as

$$A_1 = a_0, \quad A_t = 0, \quad A_2 = \frac{d_1 \cos \theta_t}{d_2 \cos(\theta_2 - \theta_t)} a_0. \quad (5.3)$$

The incident wave amplitude in (5.3) is found to remain unchanged over the patch, which is in agreement with the conservation of wave action (4.5). If (5.3) is correct, then, a bi-chromatic patch set to deflect waves by a 90° angle cannot be expected to protect the shore far from the patch's plane of symmetry. This result is now validated in figure 11 as we show the evolution in time of the envelope amplitudes over a patch infinitely long in the y -direction (and therefore the solution is independent of y) and for which $\theta_2 = \pi/2$. We provide three different cases of ripple amplitudes, i.e. $d_1/d_2 = 0.5, 1, 2$ (see figures 11(a,b,c)), in order to verify the linear relationship predicted in (5.3) between the amplitude of the deflected waves $|A_2|$ and the ratio d_1/d_2 . The incident and resonated envelope amplitudes are obtained from direct simulation and are extracted from the overall free-surface solution by fast-Fourier transform in the y -direction. We then also average in time over the carrier wave period (i.e. T_1) in order to remove the fast oscillations of the carrier wave phases. It should be noted that the wave amplitude is 0 for all three modes for $t < k_1(x - x_w)/\omega$ in figure 11 since the incident waves start propagating into the domain through the wavemaker on the left-hand-side (at $x = x_w$) only at $t = 0$.

In all cases, we see that the $\mathbf{k}_1 \leftrightarrow \mathbf{k}_t$ Bragg interaction is strongest at the initial time: $|A_t|$ increases very rapidly to the detriment of $|A_1|$ (figures 11a,b in the left and middle columns). The duration and significance of energy transfer from the \mathbf{k}_1 to the \mathbf{k}_t waves increases with increasing d_1/d_2 (i.e. from figure 11a to 11c), which is expected because the strength of the $\mathbf{k}_1 \leftrightarrow \mathbf{k}_t$ Bragg interaction is proportional to $d_1 \cos \theta_t$. Energy exchanges still occur at later times, as seen from the small oscillations of $|A_t|$, but the incident wave energy eventually becomes fully transmitted such that $|A_1|$ is as large downstream and upstream of the patch (i.e. $|A_1|/a_0 \sim 1$ at the end of the patch). The \mathbf{k}_2 wave amplitude $|A_2|$ also only increases early on, with some redistribution clearly seen across the patch at later times for the smaller d_1/d_2 (figure 11a to 11c in the right column). In particular,

we find that the plateau reached by the x averaged $|A_2|$ amplitude grows approximately linearly with d_1/d_2 , which means that (5.3) is a good first-order approximation to the y -invariant problem. That the initial net energy flow from $|A_1|$ to $|A_2|$ increases linearly with d_1/d_2 (note that the color map scales change between figures) is somewhat surprising since larger d_1 imply smaller d_2 , hence weaker $\mathbf{k}_t \leftrightarrow \mathbf{k}_2$ Bragg interactions. However, since \mathbf{k}_2 waves are *trapped* by the patch for $\theta_2 = \pi/2$, they experience an infinite number of Bragg interactions for an infinitely long patch in the y -direction. The second Bragg interaction is therefore intrinsically much more efficient than the first $\mathbf{k}_1 \leftrightarrow \mathbf{k}_t$ Bragg interaction, which becomes the limiting mechanism in the overall transfer of \mathbf{k}_1 wave energy to the \mathbf{k}_2 waves.

To summarize our results on perpendicular deflection, we found that the case of $\theta_2 = \pi/2$ offers significant wave energy reduction in the downstream near the patch's plane of symmetry. However, no protection can be obtained when $\theta_2 = \pi/2$ far from the patch's plane of symmetry, because the conservation of wave action requires waves in the downstream propagating with a non-zero velocity in the x -direction. How much far away from $y = 0$ we get the y -invariant behavior is therefore of significance importance and can be estimated, to a good first-order approximation, by inspection of the steady-state solution (5.3). Indeed, the far-field is expected to start where the deflected wave amplitude $|A_2|$ obtained for a patch with a plane of symmetry becomes as large as the y -invariant solution (5.3), i.e. at a distance $|y| > 0$ such that $|A_2(y)|/a_0 = (d_1 \cos \theta_t)/[d_2 \cos(\theta_2 - \theta_t)]$. For the results of figure 10, we find that $|A_2|$ increases approximately linearly with $|y|$. We estimated the growth slope to be ~ 0.02 per wavelength λ_1 , such that the maximum value predicted by (5.3), i.e. $|A_2|/a_0 = 3.4$, is reached at $y/\lambda_1 = 160$ in this case.

6. Conclusions

The deflection of water waves incident on a patch of oblique seabed bars has been investigated via multiple-scale analysis and direct simulations. The Bragg deflection mechanism is reliable for protecting natural coastlines, unlike the Bragg reflection mechanism, since all waves are transmitted and therefore unable to become trapped between the shoreline and the protective patch. The proposed patch of seabed corrugations for shore protection has a plane of symmetry at $y = 0$ (the y -axis is parallel to the incident wave crests, see figure 2), such that incident waves propagating in the upper half plane $y > 0$ (resp. $y < 0$) are deflected toward $y = +\infty$ (resp. $y = -\infty$). At resonance, i.e. when the incident wave frequency is equal to the Bragg frequency of the corrugated patch, the deflection of the incident waves to the sides of the patch's plane of symmetry results in a wake of decreased wave activity which is like an isosceles triangle. The extent of the protected wake in the y direction grows linearly with x (which is the direction of incident wave propagation), and can be theoretically infinite provided that the patch is likewise infinite in the y -direction. In one case, we achieved 88% wave energy reduction in a large protected wake, i.e. in an isosceles triangle with $2\theta_2 = 14\pi/15$ vertex angle. The vertex angle is twice the angle of the Bragg resonated wave (θ_2) formed with the x -axis.

The deflection of waves at or close to a 90° angle is impossible using mono-modal corrugations because the Bragg resonance condition is degenerate in this case. However, using bi-modal corrugations, we showed via multiple-scale analysis that the deflection of incident waves at a large angle is achievable provided that a transitional wave mediates the energy transfer from the incident wave mode to the target deflected wave. The corresponding resonance mechanism was referred to as a class I_2 Bragg resonance since it is a first-order two-step Bragg interaction which requires bi-modal corrugations. We derived closed form solutions for the incident and deflected waves assuming that the

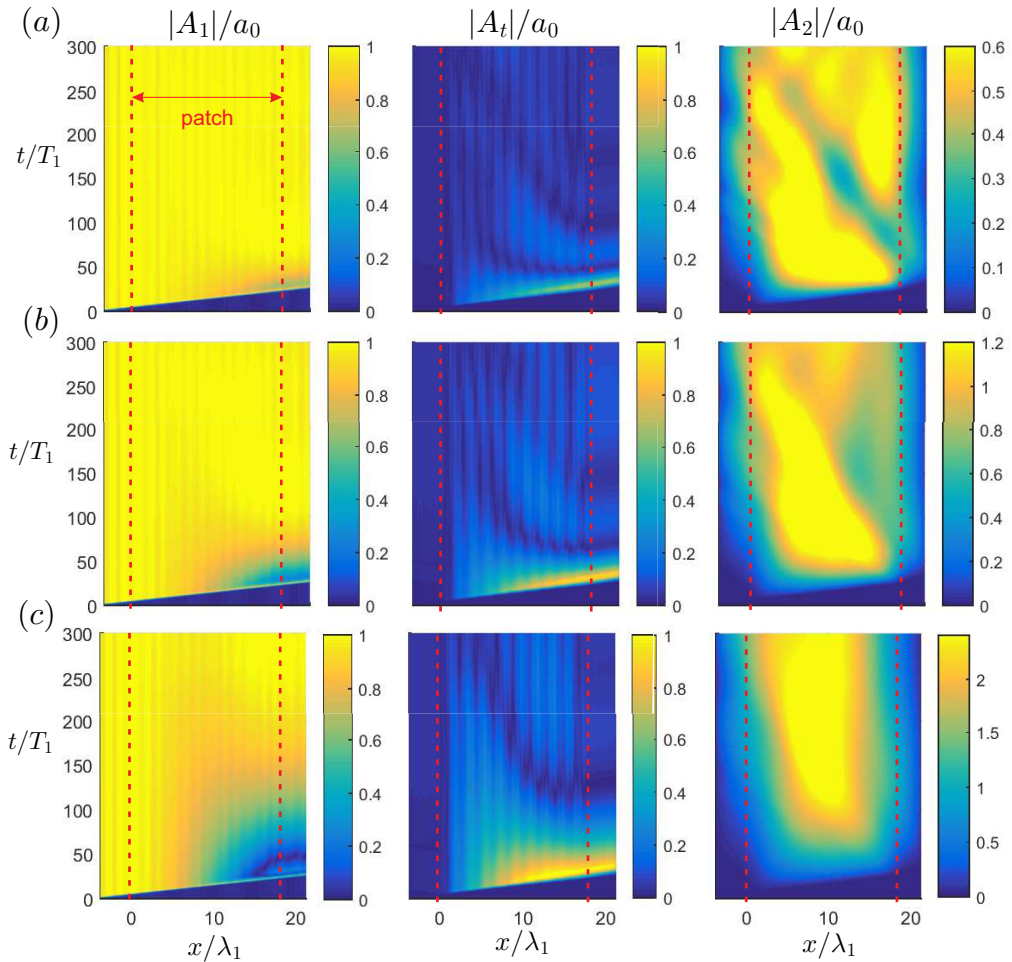


FIGURE 11. Evolution of the envelope amplitudes $|A_{1,t,2}|/a_0$ in x and t for waves incident from $x = -\infty$ and propagating over an infinitely long patch in the y -direction with $\theta_2 = 2\theta_t = \pi/2$. We consider three different distributions of ripple amplitudes: (a) $d_1/d_2 = 0.5$, (b) $d_1/d_2 = 1$, (c) $d_1/d_2 = 2$, and keep $(d_1 + d_2)/h = 0.12$ fixed. The results in the right column demonstrate that $|A_2|$ increases approximately linearly with d_1/d_2 . The patch width is $w/\lambda_1 = 17.5$ and the other physical parameters are $k_1 h = 0.2$, $a_0/h = 10^{-3}$. The direct simulation parameters are $\delta x/\lambda_1 = \delta y/\lambda_1 = 1/7.31$ and $\delta t/T_1 = 1/32$.

envelope amplitudes were invariant in the y -direction. The results allowed us to obtain the critical patch width, i.e. the patch width in the x -direction that ensures that the energy of the incident wave is fully transferred to the deflected wave.

The critical patch width has been shown to be the optimum design width for a patch with a plane of symmetry set to minimize wave activity in the target protected wake. The plane of symmetry only affects the modal wave amplitudes near the axis of symmetry and the y -invariant solution is recovered away from it. The wave-field in the protected wake is dominated by leaked beams of energy emanating near the patch's plane of symmetry. High-order spectral simulations of the full potential flow equations over a relatively large domain were shown to agree well with the results obtained from multiple-scale analysis.

The protection efficiency of the class I_2 Bragg deflection mechanism has been shown to be relatively robust to small frequency detuning. The effect of detuning, nevertheless, has

a cumulative effect for class I_2 since the secondary Bragg interactions are more strongly affected than first-step interactions. As a result, detuning has a stronger negative effect on the protection efficiency in the case of the class I_2 (bi-chromatic patch) than in the case of class I (a monochromatic patch). For incident waves propagating at an angle with respect to the normal-to-shore direction, the wavenumber vector can be written as $\mathbf{k}_1 + \kappa(\hat{x} \cos \beta + \hat{y} \sin \beta)$ where \mathbf{k}_1 is the Bragg resonant wavenumber. We thus see that the effect on the protection efficiency of small oblique incidence (which implies $\kappa \ll k_1$), generally negligible nearshore due to refraction, is similar to that of frequency detuning (c.f. Kirby 1993).

In the case of perpendicular deflection, when the incident and final resonated waves are perpendicular, we found that the incident wave energy stops flowing to the deflected waves far from the patch's plane of symmetry after relatively short transients. As a result, the protection offered by a patch set to deflect waves at a 90° angle is of limited extent in the y -direction, and restricted to the neighborhood of the patch's plane of symmetry. Perpendicular deflection also results in leaked waves, which, once reflected by a shoreline, can excite waves propagating along the patch in a way that water-wave trapping becomes again possible. This is, of course, an undesirable feature as explained by Yu & Mei (2000a) for the case of shore-parallel seabed bars. The formation of waves that propagate parallel to the patch may be, however, relevant to the analysis of topographically-trapped waves, aka Bloch waves, as the excitation of such waves by free modes remains of contemporary interests (c.f. Porter & Porter 2001).

While longshore natural sandbars can survive under natural wave loading conditions (as shown by e.g. Yu & Mei 2000b; Kriebel & Dean 1985), oblique sandbars may prove to be more fragile. The possibility to observe the class I_2 Bragg interaction in the natural environment as well as the survivability of man-made protective patches based on oblique seabed bars thus call for appropriate erosion and dynamic loads studies.

Appendix I

The evolution of the incident and resonated wave amplitudes $A_{1,t,2}$ over a bichromatic patch with corrugations ζ given by (4.1) can be found using multiple scales by considering a first-order potential $\phi^{(1)}$ of the form

$$\phi^{(1)} = \alpha_1(z)e^{i(\mathbf{k}_1 \cdot \mathbf{x} - \omega t)} + \alpha_t(z)e^{i(\mathbf{k}_t \cdot \mathbf{x} - \omega t)} + \alpha_2(z)e^{i(\mathbf{k}_2 \cdot \mathbf{x} - \omega t)} + cc, \quad (6.1)$$

where

$$\alpha_j(z; \bar{x}, \bar{y}, \bar{t}) = \frac{A_j(\bar{x}, \bar{y}, \bar{t})}{2} \frac{g}{\omega} \frac{\cosh[k_1(z+h)]}{\cosh(k_1 h)}, \quad j = 1, t, 2. \quad (6.2)$$

The equation for $A_{1,t,2}$ can then be obtained from the solvability condition which ensures that a bounded second-order potential of the form

$$\phi^{(2)} = \psi_1(z)e^{i(\mathbf{k}_1 \cdot \mathbf{x} - \omega t)} + \psi_t(z)e^{i(\mathbf{k}_t \cdot \mathbf{x} - \omega t)} + \psi_2(z)e^{i(\mathbf{k}_2 \cdot \mathbf{x} - \omega t)} + \textit{locked waves} + cc, \quad (6.3)$$

satisfies the second-order problem. In (6.3), the slow variations of the amplitudes $\psi_{1,t,2}$ only affect the third-order solution and, as a result, they can be neglected in the present derivation. The expression *locked waves* designates non-resonating terms of the second-order solution which do not play any role in obtaining the evolutionary equations for $A_{1,t,2}$. At the second order $\mathcal{O}(\epsilon^2)$ in bottom steepness, the governing equations obtained neglecting wave-wave interactions read

$$\nabla^2 \phi^{(2)} + (\nabla_h \cdot \bar{\nabla} + \bar{\nabla} \cdot \nabla_h) \phi^{(1)} = 0, \quad \text{in } -h \leq z \leq 0, \quad (6.4a)$$

$$\phi_{tt}^{(2)} + g\phi_z^{(2)} + 2\phi_{t\bar{t}}^{(1)} = 0, \quad \text{on } z = 0, \quad (6.4b)$$

$$\epsilon\phi_z^{(2)} = -\epsilon\bar{\nabla}h \cdot \nabla_h\phi^{(1)} + \nabla_h \cdot (\zeta\nabla_h\phi^{(1)}), \quad \text{on } z = -h, \quad (6.4c)$$

where $\bar{\nabla} = (\partial_{\bar{x}}, \partial_{\bar{y}})$. In (6.4a), we note that $\bar{\nabla}$ and ∇_h do not commute because of the simultaneous fast and slow spatial variations of the wave phases. Substituting (6.1) and (6.3) in (6.4) we have for each wave mode, i.e. for $j = 1, t, 2$,

$$\psi_{j,zz} - k_1^2\psi_j = -i[\bar{\nabla} \cdot (\mathbf{k}_j\alpha_j) + \mathbf{k}_j \cdot \bar{\nabla}\alpha_j], \quad \text{in } -h \leq z \leq 0, \quad (6.5a)$$

$$-\omega^2\psi_j + g\psi_{j,z} = 2i\omega\alpha_{j,\bar{t}}, \quad \text{on } z = 0, \quad (6.5b)$$

$$\epsilon\psi_{j,z} = \gamma_{jm}\alpha_m - i\epsilon(\bar{\nabla}h) \cdot (\mathbf{k}_j\alpha_j), \quad \text{on } z = -h, \quad (6.5c)$$

where Einstein summation is implied for repeated indices and with $\gamma_{11} = \gamma_{12} = \gamma_{tt} = \gamma_{21} = \gamma_{22} = 0$, and $\gamma_{1t} = \gamma_{t1} = -(d_1/2)\mathbf{k}_1 \cdot \mathbf{k}_t$, $\gamma_{t2} = \gamma_{2t} = -(d_2/2)\mathbf{k}_t \cdot \mathbf{k}_2$. Since the α_j are the homogeneous solutions of (6.5), the forced system (6.5) admits non-trivial solutions ψ_j if and only if a so-called compatibility condition is satisfied (Fredholm 1903; Mei 1985). Applying Green's second identity, with asterisks denoting complex conjugates, the solvability condition can be cast into

$$\int_{-h}^0 dz [\alpha_j^*(\psi_{j,zz} - k_1^2\psi_j) - \psi_j(\alpha_{j,zz}^* - k_1^2\alpha_j^*)] = \left[\alpha_j^* \frac{\partial\psi_j}{\partial z} - \psi_j \frac{\partial\alpha_j^*}{\partial z} \right]_{-h}^0, \quad (6.6)$$

which, after some manipulations, reduces to a system of coupled partial-differential equations for the slowly varying wave envelopes, i.e.,

$$A_j^* \epsilon \frac{\partial}{\partial t} A_j + \frac{1}{2} A_j^* \epsilon \bar{\nabla} \cdot (\mathbf{C}_{\mathbf{g}_j} A_j) + \frac{1}{2} A_j^* \mathbf{C}_{\mathbf{g}_j} \cdot \epsilon \bar{\nabla} A_j = i A_j^* \begin{cases} A_t \Omega_1, & j = 1 \\ A_1 \Omega_1 + A_2 \Omega_2, & j = t \\ A_t \Omega_2, & j = 2 \end{cases} \quad (6.7)$$

with $\mathbf{C}_{\mathbf{g}_j}$, and Ω_1 and Ω_2 given in (3.4) and (4.4). Summing all three partial-differential equations (6.7) together with their complex conjugate counterparts yields the well-known conservation law of wave action, i.e. equation (4.5). Equation (6.7) can then be readily simplified into equation (4.3) by dividing by A_j^* . Equation (6.7) (or (4.3)) further reduces to equations (2.33)-(2.34) of Mei (1985) for a single bottom corrugation ($d_2 = 0 \Rightarrow \Omega_2 = 0$) and upon substitution of (A_1, A_t) with $(A^+, -A^-)$.

Appendix II

The effect of detuning on the modulation of the envelope amplitudes is here investigated for an infinitely long patch in the y -direction. We solve the multiple-scale system of equations (4.3) analytically assuming $\partial/\partial\bar{y} = 0$ and replacing $\partial/\partial\bar{t}$ by $-i\varpi$ where $\omega = \omega_1 + \varpi$ is the incident wave frequency and ϖ is the detuning frequency. Figure 12 shows the normalized wave amplitudes for different detuning parameters. With no detuning (solid lines), we see that the \mathbf{k}_1 wave energy is fully transferred to the \mathbf{k}_2 wave mode at $x_n = (2n+1)\omega_{cr_2}$ for every $n \in \mathbb{N}$ (c.f. (4.6) with (4.8) satisfied). With detuning, however, full energy transfer cannot be achieved because (4.8) is no longer satisfied, the critical patch width changes, and the Bragg interactions are weaker. Interestingly, detuning first results in an increase of energy flowing to the transitional mode \mathbf{k}_t . Indeed, detuning affects more importantly the second interaction of the 2-step Bragg mechanism, such that more energy can be stored into the \mathbf{k}_t waves. For larger detuning, however, both the first and second interactions weaken such that the incident wave amplitude becomes barely affected by the corrugations. Figure 13 finally shows the minimum of a_1^* , as well as the maximum of a_t^* and a_2^* , as a function of ϖ/ω_1 for different parameters $k_1 h$. Clearly,

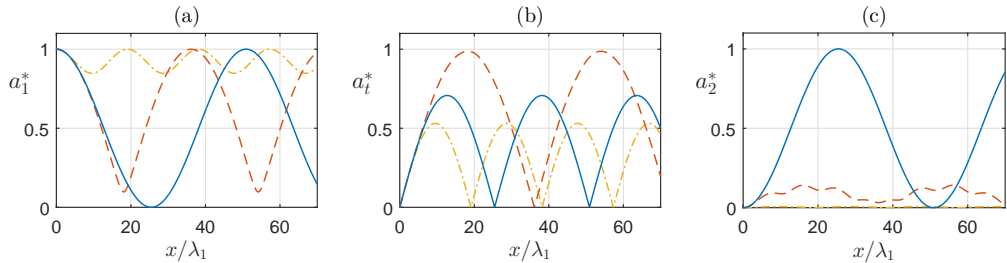


FIGURE 12. Normalized envelope amplitudes of the (a) incident, (b) transitional and (c) target modes over a bi-chromatic patch infinitely long in the y -direction with no detuning ($\varpi = 0$, solid lines), some detuning ($\varpi = 0.01\omega_1$ or $\varpi = 0.66\Omega_{12}$, dash-dash lines), large detuning ($\varpi = 0.1\omega_1$ or $\varpi = 6.6\Omega_{12}$, dash-dot lines). The physical parameters are $k_1 = 70$, $\theta_2 = 7\pi/15$, $\theta_t = \theta_2/2$, $k_1 h = 1$, $a_0/h = 10^{-3}$, $(d_1 + d_2)/h = 0.12$, with (4.8) satisfied.

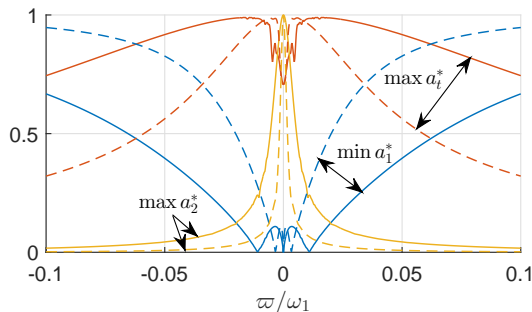


FIGURE 13. Minimum of the normalized incident wave amplitude a_1^* and maximum of the normalized resonated wave amplitudes, i.e. a_t^* and a_2^* , as a function of detuning ϖ/ω_1 where ω_1 is the perfectly tuned wave frequency, for a patch semi-infinitely wide in the x -direction and infinitely long in the y -direction. The results are shown for both relatively long (i.e. $k_1 h = 0.2$, solid lines) and short (i.e. $k_1 h = 1.5$, dash-dash lines) waves. The effect of detuning is clearly stronger for the shorter waves. Other physical parameters are as in figure 12.

as mentioned in §5.2, the parameter ϖ/ω_1 has a stronger effect on short waves than on long waves, and the second resonated mode a_2^* is more affected than the transitional mode a_t^* .

REFERENCES

- ALAM, M.-R. 2012a Broadband Cloaking in Stratified Seas. *Physical Review Letters* **108** (8), 084502.
- ALAM, M.-R. 2012b A flexible seafloor carpet for high-performance wave energy extraction. In *ASME 2012 31st International Conference on Ocean, Offshore and Arctic Engineering*, pp. 839–846. American Society of Mechanical Engineers.
- ALAM, M.-R., LIU, Y. & YUE, D. K. P. 2009a Bragg resonance of waves in a two-layer fluid propagating over bottom ripples. Part II. Numerical simulation. *Journal of Fluid Mechanics* **624**, 225.
- ALAM, M.-R., LIU, Y. & YUE, D. K. P. 2009b Waves due to an oscillating and translating disturbance in a two-layer density-stratified fluid. *Journal of Engineering Mathematics* **65** (2), 179–200.
- ALAM, M.-R., LIU, Y. & YUE, D. K. P. 2010 Oblique sub- and super-harmonic Bragg resonance of surface waves by bottom ripples. *Journal of Fluid Mechanics* **643**, 437.

- ALAM, M.-R., LIU, Y. & YUE, D. K. P. 2011 Attenuation of short surface waves by the sea floor via nonlinear sub-harmonic interaction. *Journal of Fluid Mechanics* **689**, 529–540.
- ATHANASSOULIS, G. A. & BELIBASSAKIS, K. A. 1999 A consistent coupled-mode theory for the propagation of small-amplitude water waves over variable bathymetry regions. *Journal of Fluid Mechanics* **389**, 275–301.
- BAILARD, J. A., DEVRIES, J. W. & KIRBY, J. T. 1992 Considerations in using Bragg reflection for storm erosion protection. *Journal of Waterway, Port, Coastal, and Ocean Engineering* **118** (1), 62–74.
- BAILARD, J. A., DEVRIES, J. W., KIRBY, J. T. & GUZA, R. T. 1990 Bragg Reflection Breakwater: A New Shore Protection Method? In *Coastal Engineering Proceedings*, pp. 1702–1715.
- BELIBASSAKIS, K. A., ATHANASSOULIS, G. A. & GEROSTATHIS, T. P. 2001 A coupled-mode model for the refraction-diffraction of linear waves over steep three-dimensional bathymetry. *Applied Ocean Research* **23** (6), 319–336.
- COUSTON, L.-A., GUO, Q., CHAMANZAR, M. & ALAM, M.-R. 2015 Fabry-Perot resonance of water waves. *Physical Review E* **043015**, 1–7.
- DAVIES, A. G. 1982 The reflection of wave energy by undulations on the seabed. *Dynamics of Atmospheres and Oceans* **6**, 207–232.
- DAVIES, A. G. & HEATHERSHAW, A. D. 1984 Surface-wave propagation over sinusoidally varying topography. *Journal of Fluid Mechanics* **144**, 419–443.
- DOMMERMUTH, D. G. & YUE, D. K. P. 1987 A high-order spectral method for the study of nonlinear gravity waves. *Journal of Fluid Mechanics* **184**, 267–288.
- ELGAR, S., RAUBENHEIMER, B. & HERBERS, T. H. C. 2003 Bragg reflection of ocean waves from sandbars. *Geophysical Research Letters* **30** (1), 3–6.
- EMANUEL, K. 2005 Increasing destructiveness of tropical cyclones over the past 30 years. *Nature* **436** (7051), 686–688.
- FREDHOLM, I. 1903 Sur une classe d'équations fonctionnelles. *Acta Mathematica* **27** (1), 365–390.
- GUAZZELLI, E., REY, V. & BELZONS, M. 1992 Higher-order Bragg reflection of gravity surface waves by periodic beds. *Journal of Fluid Mechanics* **245**, 301.
- HEATHERSHAW, A. D. 1982 Seabed-wave resonance and sand bar growth. *Nature* **296** (25), 343–345.
- HOWARD, L. N. & YU, J. 2007 Normal modes of a rectangular tank with corrugated bottom. *Journal of Fluid Mechanics* **593**, 209–234.
- INMAN, D. L. & DOLAN, R. 1989 The outer banks of north carolina: Budget of sediment and inlet dynamics along a migrating barrier system. *Journal of Coastal Research* pp. 193–237.
- KIRBY, J. T. 1986 A general wave equation for waves over rippled beds. *Journal of Fluid Mechanics* **162**, 171–186.
- KIRBY, J. T. 1993 A note on Bragg scattering of surface waves by sinusoidal bars. *Physics of Fluids A: Fluid dynamics* **5**, 380–386.
- KIRBY, J. T. & ANTON, J. P. 1990 Bragg reflection of waves by artificial bars. In *Coastal Engineering Proceedings*, pp. 757–768.
- KRIEBEL, D. L. & DEAN, R. G. 1985 Numerical simulation of time-dependent beach and dune erosion. *Coastal Engineering* **9**, 221–245.
- LIU, P. L.-F., YEH, H., LIN, P., CHANG, K.-T. & CHO, Y.-S. 1998 Generation and evolution of edge-wave packets. *Physics of Fluids* **10** (7), 1635.
- LIU, Y. & YUE, D. K. P. 1998 On generalized Bragg scattering of surface waves by bottom ripples. *Journal of Fluid Mechanics* **356**, 297–326.
- MADSEN, PER A., FUHRMAN, D. R. & WANG, B. 2006 A Boussinesq-type method for fully nonlinear waves interacting with a rapidly varying bathymetry. *Coastal Engineering* **53** (5–6), 487–504.
- MAGNE, R., REY, V. & ARDHUIN, F. 2005 Measurement of wave scattering by topography in the presence of currents. *Physics of Fluids* **17** (12).
- MEI, C. C. 1985 Resonant reflection of surface water waves by periodic sandbars. *Journal of Fluid Mechanics* **152**, 315–335.
- MEI, C. C., HARA, T. & NACIRI, M. 1988 Note on Bragg scattering of water waves by parallel bars on the seabed. *Journal of Fluid Mechanics* **186**, 147–162.

- MITRA, A. & GREENBERG, M. D. 1984 Slow Interactions of Gravity Waves and a Corrugated Sea Bed. *Journal of Applied Mechanics* **51** (251), 5–9.
- NACIRI, M. & MEI, C. C. 1988 Bragg scattering of water waves by a doubly periodic seabed. *Journal of Fluid Mechanics* **192** (-1), 51.
- O'HARE, T. J. & DAVIES, A. G. 1992 A new model for surface wave propagation over undulating topography. *Coastal Engineering* **18** (3-4), 251–266.
- PINSKER, Z. G. 1978 *Dynamical Scattering of X-rays in Crystals*, , vol. 3. Springer-Verlag Berlin.
- PORTER, D. & STAZIKER, D. J. 1995 Extensions of the mild-slope equation. *Journal of Fluid Mechanics* **300**, 367–382.
- PORTER, R. & PORTER, D. 2001 Interaction of water waves with three-dimensional periodic topography. *Journal of Fluid Mechanics* **434**, 301–335.
- SEO, S. N. 2014 Transfer matrix of linear water wave scattering over a stepwise bottom. *Coastal Engineering* **88**, 33–42.
- TOFFOLI, A., GRAMSTAD, O., TRULSEN, K., MONBALIU, J., BITNER-GREGERSEN, E. & ONORATO, M. 2010 Evolution of weakly nonlinear random directional waves: laboratory experiments and numerical simulations. *Journal of Fluid Mechanics* **664**, 313–336.
- WEBSTER, P. J., HOLLAND, G. J., CURRY, J. A. & CHANG, H.-R. 2005 Changes in tropical cyclone number, duration, and intensity in a warming environment. *Science (New York, N.Y.)* **309** (5742), 1844–6.
- WEIDMAN, P. D., HERCZYNSKI, A., YU, J. & HOWARD, L. N. 2015 Experiments on standing waves in a rectangular tank with a corrugated bed. *Journal of Fluid Mechanics* **777**, 122–150.
- WEST, B. J., BRUECKNER, K. A., JANDA, R. S., MILDER, D. M. & MILTON, R. L. 1987 A new numerical method for surface hydrodynamics. *Journal of Geophysical Research* **92** (C11), 11803–11.
- YU, J. & HOWARD, L. N. 2012 Exact Floquet theory for waves over arbitrary periodic topographies. *Journal of Fluid Mechanics* **712**, 451–470.
- YU, J. & MEI, C. C. 2000*a* Do longshore bars shelter the shore? *Journal of Fluid Mechanics* **404**, 251–268.
- YU, J. & MEI, C. C. 2000*b* Formation of sand bars under surface waves. *Journal of Fluid Mechanics* **416**, 315–348.
- ZAKHAROV, V. E. 1968 Stability of Periodic Waves of Finite Amplitude on the Surface of Deep Fluid. *J. Appl. Mech. Tech. Phys.* **9** (2), 190–194.